

Antiparallel versus component merging at the magnetopause: Current bifurcation and intermittent reconnection

Homa Karimabadi

Department of Electrical and Computer Engineering, University of California, San Diego, La Jolla, California, USA

William Daughton¹

Department of Physics and Astronomy, University of Iowa, Iowa City, Iowa, USA

Kevin B. Quest

Department of Electrical and Computer Engineering, University of California, San Diego, La Jolla, California, USA

Received 16 August 2004; revised 24 November 2004; accepted 23 December 2004; published 17 March 2005.

[1] One of the major unresolved issues regarding magnetic reconnection at the dayside magnetopause is the location where reconnection first occurs during periods of a large interplanetary magnetic field B_y . In order to address this issue, we examine and contrast the onset of reconnection in the presence and absence of a finite guide field (B_y). In an accompanying paper (Karimabadi et al., 2005) we showed that in case of one linearly unstable mode, tearing saturates at amplitudes too small to be of relevance to transport at the magnetopause, even in the antiparallel case. However, we show that in general a number of modes are simultaneously unstable at the magnetopause. This process is aided by the presence of electron temperature anisotropy which broadens the unstable spectrum, extending it to very short wavelengths. Multimode tearing gets past the single mode stabilization and grows to large amplitudes in several stages: the initial linear stage, the coalescence process which proceeds at a slower growth rate, the growth and dominance of the longest wavelength in the system, and a final explosive phase which leads to a saturated state with a bifurcated current sheet. The aspect ratio of the magnetic island at the end of the explosive phase is ~ 0.2 . This is in good agreement with the aspect ratio of the magnetic island structure at Earth's magnetopause reconstructed from the single-spacecraft data by Hau and Sonnerup (1999). We find that in addition to coalescence, there can occur stretching of the X lines. This leads to a recurrent reconnection process where only a single, rather than a pair of magnetic structures are periodically produced, reminiscent of flux transfer events. Although the detailed properties of the various interacting modes are altered in the presence of a guide field, the basic scenario including the final explosive phase of the system remains even for very large guide fields. We calculate the steady state reconnection rate as a function of guide field and plasma beta and show that fast reconnection is obtained even for modest values of guide field. Detailed application of these results to the magnetopause is discussed. One key finding is that it takes a very weak guide field of less than 0.07 of the magnetosheath field to transition away from the antiparallel reconnection. The linear growth rate of isotropic tearing compared to convection time is fast only for thin sheets. In the absence of electron temperature anisotropies, both antiparallel and component merging remain competitive as long as the guide field is not too strong (≤ 0.4). Local condition, most importantly the shear flow, is identified as one effect that may change the behavior of reconnection in the antiparallel versus component merging.

Citation: Karimabadi, H., W. Daughton, and K. B. Quest (2005), Antiparallel versus component merging at the magnetopause: Current bifurcation and intermittent reconnection, *J. Geophys. Res.*, 110, A03213, doi:10.1029/2004JA010750.

¹Also at Los Alamos National Laboratory, Los Alamos, New Mexico, USA.

1. Introduction

[2] One of the controversial issues regarding magnetic reconnection at the magnetopause is the location of the reconnection line on the dayside magnetopause during periods of a large interplanetary magnetic field B_y . The

antiparallel merging model [Crooker, 1979; Luhmann *et al.*, 1984] predicts that reconnection would occur where the magnetic shear across the magnetopause is largest and predicts no reconnection in the subsolar region when the IMF B_y (the so-called guide field) is large. In contrast, the component merging model [Sonnerup, 1974; Gonzalez and Mozer, 1974] predicts that the reconnection line passes through the subsolar point and has an orientation that is controlled by the IMF. As we discussed in an accompanying paper [Daughton and Karimabadi, 2005, hereinafter referred to as Paper I], the results from observations of magnetopause as well as theories of reconnection have been inconclusive. In order to address the issue of reconnection onset at the magnetopause, we have used a combination of linear theory and high-resolution simulations to compare and contrast the efficiency of collisionless reconnection in the antiparallel (zero guide field) and component merging (finite guide field) geometries. Paper I examined the detailed properties of the tearing mode as a function of guide field strength. It was found that the properties of tearing mode can be categorized into three regimes depending on whether the guide field B_y is smaller or larger than a characteristic guide field given by

$$\frac{B_y^*}{B_{x0}} \equiv \frac{1}{\sqrt{2}} \left(\frac{\rho_i}{L} \right)^{1/2} \left(\frac{T_e m_e}{T_i m_i} \right)^{1/4}.$$

Here

$$\rho_i = \frac{m_i c}{e B_{x0}} v_{ti}$$

is the ion gyroradius, v_{ti} is the ion thermal velocity $(2T_i/m_i)^{1/2}$, and L is the current sheet half-thickness. The three parameter regions are (1) the weak guide field regime $B_{y0} < B_y^*$ which includes the zero guide field as a special case, (2) the strong guide field limit $B_{y0} > 3B_y^*$, and (3) in between these two limits, there exists a previously unknown regime that we refer to as the intermediate regime $3B_y^* \gtrsim B_{y0} > B_y^*$ where tearing has unusual properties such as maximum growth at oblique angles. Finally, we showed that changing the guide field from 0 to a value equal to the main field reduces the growth rate by a factor of ~ 3.75 . Thus we concluded that component merging cannot be ruled out based on linear theory of tearing.

[3] Given this result, the next obvious question is whether there are significant differences in the nonlinear evolution of the tearing mode between the zero guide field and finite guide field configurations. However, a theoretical study of saturation for these two limits has not been done systematically and previous works have yielded contradictory results. In the second paper in this series [Karimabadi *et al.*, 2005, hereinafter referred to as Paper II], we considered the nonlinear evolution of the tearing mode in the presence of one unstable mode. We found that a single tearing mode saturates at too small of an amplitude to be of relevance at the magnetopause. Here we extend this calculation to the case of multiple unstable modes.

[4] There exist several previous works that dealt with the nonlinear evolution of tearing in the presence of multimodes but in the absence of a guide field. In the collisionless limit,

Biskamp et al. [1970] used quasilinear theory to conclude that tearing would saturate at amplitudes much smaller than the singular layer thickness. *Malara et al.* [1992], using incompressible MHD, found that unlike the single mode case, the saturation occurs due to inverse energy cascade (i.e., coalescence in the physical space). The coalescence process takes away energy from the tearing unstable modes, resulting in their saturation. However, the longest wavelengths continue to grow and achieve amplitudes much larger than those predicted by *Biskamp et al.* [1970]. A one-species simulation of the tearing mode in the presence of multiple unstable modes by *Pritchett* [1992] also revealed an explosive growth, following the coalescence phase (see also earlier papers such as *Leboeuf et al.* [1982]). *Pritchett* attributed the explosive growth to the vacuum effect. It is interesting to note, however, that the explosive growth phase has not been observed in the fluid simulations of tearing [e.g., *Malara et al.*, 1992].

[5] The saturation mechanism of the tearing mode in the presence of a guide field is even less understood. Early theoretical studies ruled out component-merging as a possibility. The physics behind the stabilization of guide field tearing is the modification of resonant particle orbits by the growing island. Taking into account the influence of the perturbed electron orbits, it was shown [e.g., *Drake and Lee*, 1977; *Coroniti and Quest*, 1984] that the single tearing mode saturates at minute amplitudes (~ 50 m), much smaller than the magnetopause current layer thickness of 50–200 km. In Paper II, we showed that these theories underestimate the saturation amplitude, but even with the corrected estimates, single mode tearing saturates at small amplitudes (~ 9 –36 km). Magnetic field line stochasticity was considered as a way to obtain larger saturation amplitudes [e.g., *Galeev et al.*, 1986, and references therein]. The overlap of neighboring magnetic islands can lead to destruction of magnetic surfaces, allowing the field lines to percolate through the magnetopause boundary layer. However, this diffusion process is too slow and may lead to saturation amplitude that is at most 3–4 times larger than the single tearing mode case [Wang and Ashour-Abdalla, 1994].

[6] In this paper, we use two-dimensional full particle and hybrid (electron fluid, kinetic ions) simulations to examine in detail the nonlinear evolution of multimode tearing instability as a function of the guide field. The remainder of this paper is organized as follows. Section 2 includes the simulations model. Section 3 presents the simulation results and our new theory for the saturation mechanism for the antiparallel geometry. Section 4 includes a description of nonlinear theories of the guide field tearing, followed by our simulation results. Section 5 pools the results from sections 3–4 and uses them to address the issue of antiparallel versus component merging at the magnetopause. The reader interested only in the application to the magnetotail can skip the first three sections and go directly to section 5. Summary and conclusion follow in section 6.

2. Simulation Model

[7] The simulation model is based on the Harris equilibrium [Harris, 1962] and is identical to that used in Paper II. We use two types of simulations, the full particle and electromagnetic hybrid code. The reader is referred to Paper

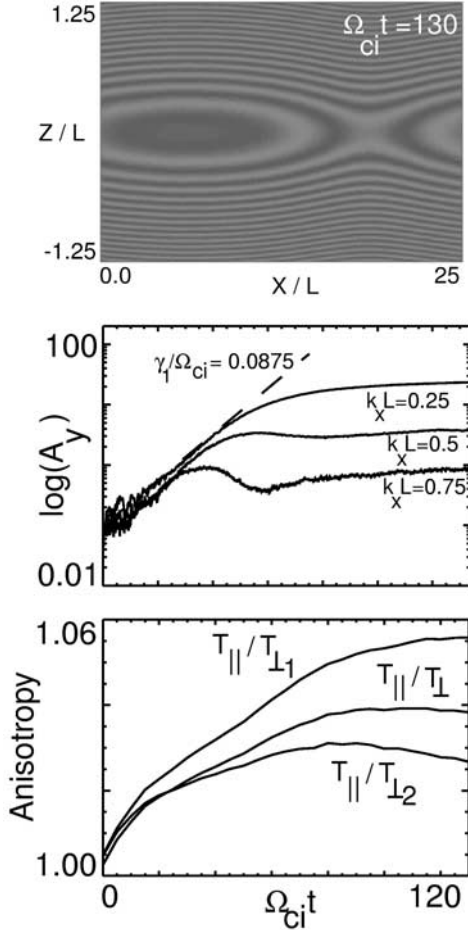


Figure 1. Harris run with three unstable modes. (a) Contour of the vector potential A_y . (b)–(c) Time evolution of the modes as well as the electron temperature anisotropy. See color version of this figure in the HTML.

II and *Karimabadi et al.* [2004a] for discussions of the full particle and hybrid codes, respectively. The hybrid algorithm is based on a modified version of the one-pass algorithm that has superior performance over other methods for reconnection problems [*Karimabadi et al.*, 2004a].

3. Antiparallel Reconnection

[8] In order to examine the effect of multiple unstable modes, we have performed two simulations with the same parameters as in run 2 in Table 2 in Paper II ($m_i/m_e = 100$, $\omega_{pe}/\omega_{ce} = 5$, $T_i/T_e = 1$, $\rho_i/L = 1.0$), except here we have doubled (three linearly unstable modes) and quadrupled (six linearly unstable modes) the size of the system in the x -

direction, which is along the magnetic field. We have also increased the size of the simulation box in the z -direction in order to accommodate the larger size of the magnetic island. Here ρ_i is the ion gyroradius

$$\rho_i = \frac{m_i c}{e B_{x0}} v_{ti},$$

v_{ti} is the ion thermal velocity $(2T_i/m_i)^{1/2}$, ω_{pe} is the electron plasma frequency, and ω_{ce} is the electron gyrofrequency.

[9] Figure 1 shows the results for the case where there are three linearly unstable modes in the system. The simulation consists of 640×1280 cells, cell spacing of $\sim 0.14 c/\omega_{pe}$ in each direction, with 50 million particles per species, and a time step of $\omega_{ce}\Delta t = 0.05$. The size of the island has now increased by about 69% (Table 1), compared with the one-mode case, to $\sim 0.44 L$ while the temperature anisotropy levels are similar to the one-mode case. In the remainder of this paper we will use the definitions $T_{\parallel}/T_{\perp 1} = T_{e_y}/T_{e_z}$ and $T_{\parallel}/T_{\perp 2} = T_{e_y}/T_{e_x}$ and whenever we refer to temperature anisotropy, it is meant to be the electron temperature anisotropy. Thus the presence of three unstable modes has allowed the system to get past the single mode stabilization. Initially, all three modes grew with mode $k_x L = 0.25$ growing at its linear rate but the other two modes grew at a slower rate compared with their linear rates (Table 2). As these modes grow, three islands are formed (not shown) but soon the two shortest modes in the system saturate and the longest mode ($k_x L = 0.25$) remains, giving rise to one island as shown in Figure 1. The saturation amplitude at the end of the linear phase is about $0.4 L$ which is very close to its final value of $\sim 0.44 L$. Thus coalescence is not energetically important and its main role is in transferring energy from short to long wavelengths while affecting only moderate change in the total fluctuation energy [see also *Pritchett*, 1992, and references therein].

[10] Next, we consider the case where there are seven linearly unstable modes in the system. The simulation consists of 640×2560 cells, cell spacing of $\sim 0.14 c/\omega_{pe}$ in each direction, with 100 million particles per species, and a time step of $\omega_{ce}\Delta t = 0.05$. The linear growth rate for the seven modes and their measured value from the simulation are listed in Table 2. All six modes except for modes 5 and 7 initially grow (Figure 2), giving rise to six islands at early time, but since mode 4 has the fastest growth rate, the system rapidly evolves to four islands. In Figure 2b we have fitted the growth curve of mode 1 with exponential functions with differing growth rates at different times during its evolution. Also indicated in this figure is the magnetic island width at the end of each time segment. The simulation was stopped before the system reached full saturation. The nonlinear evolution of this system is clearly more complex than the case with three unstable modes (Figure 1). We have

Table 1. Comparison Between Theoretical and Observed Saturation Amplitudes for Four Runs

	Analytical Theory of <i>Drake and Lee</i> [1977]	w_s/L	Singular Layer Thickness	ρ_e/L	$[c/\omega_{pe}]/L$	$[c/\omega_{pi}]/L$
Harris-1		0.26	0.40	0.1	0.14	1.4
Harris-3		0.44	0.40	0.1	0.14	1.4
Guide-1	0.017	0.24	0.45	0.17	0.14	1.4
Guide-3		0.43	0.45	0.17	0.14	1.4

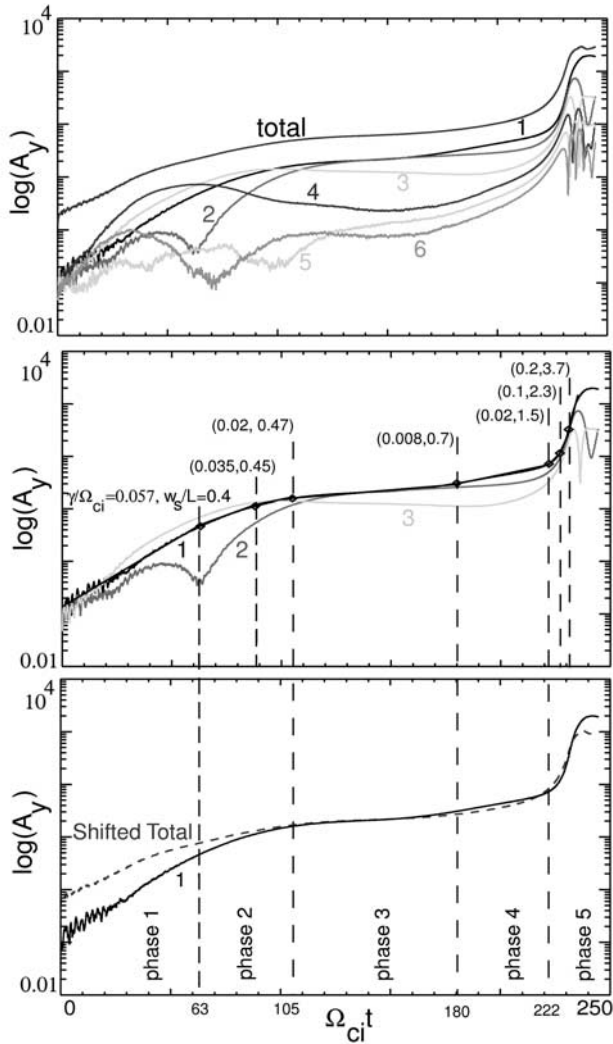


Figure 2. Harris run with seven unstable modes. (a) Time evolution of modes 1–7 as well as the sum of all the modes. (b) Fitting of the growth curve of mode 1 with exponential growth curves. Also shown is the island amplitude at each interval. (c) Identification of the different phases in the time evolution of the collisionless tearing mode. We have also plotted the total A_y (summed over all the modes) and shifted it down for a better comparison with the growth curve of mode 1. See color version of this figure in the HTML.

overlaid the growth curve of mode 1 and the total fluctuating energy in Figure 2c. Using Figures 2b–2c, we have identified five phases in the evolution of the tearing mode. Phase 1 involves the initial linear growth of the modes. During this phase, mode 1 grows at very close to its predicted linear rate, but mode 4 and 3 have the largest amplitudes due to their larger growth rate. Phase 2 is the beginning of a long, slow coalescence process where the power shifts from shorter wavelengths (modes 3 and 4) to longer wavelengths (modes 1 and 2). The growth of mode 1 has slowed down significantly in phase 2 but at the end of phase 2, mode 1 has comparable amplitude to modes 2 and 3. The island width at the end of this phase is comparable to the saturation amplitude of the three-mode case above but here

the longest wavelength in the system (mode 1) continues to grow, albeit at a very slow rate. During phase 3, mode 1 and 2 have become the dominant modes in the system and the island has grown to almost twice its value at the end of phase 1. Coalescence process is not energetically significant. Its main effect is in driving the longest wavelengths in the systems past the stabilizing influences of the electrons and into the ion regime at which point fast reconnection can take place. Figure 2c shows that mode 1 is growing at a faster rate than the total fluctuating energy during phase 4 but the situation is reversed in phase 5. The reason is that in phase 4 the shorter wavelength modes start to grow but mode 3 loses power, reducing the total fluctuating energy but in phase 5 all modes grow. Coalescence process shifts power from short to long wavelengths but in phase 4, even short wavelength modes start to grow. This indicates that the evolution of the system is not a simple coalescence process during this phase. We explain this effect as being due to ion physics as we will shortly demonstrate, using hybrid simulations. The island width during this phase has approached the ion Larmor radius and thus ions are starting to play a role in the evolution of the system. The final stage consists of an explosive phase where mode 1 grows at close to 4 times its linear rate and leads to an island width that is almost a factor of 10 larger. The explosive phase has been reported previously [e.g., *Terasawa, 1981; Pritchett, 1992*] and has been attributed to the formation of a vacuum X region. We will get back to this point shortly. Note that the island amplitude at the end of the run is several orders of magnitude larger than that predicted by *Biskamp et al. [1970]*.

[11] Although the nonlinear evolution shown in Figure 2 shows some similarities to that reported by *Malara et al. [1992]*, there are differences in the late time evolution of the system. The most important difference is that *Malara et al.* did not observe the formation of the vacuum reconnection (phase 5). As we show below, we get fast reconnection leading to a near vacuum state even with our hybrid code which uses a localized resistivity. Thus the most likely cause is the use of incompressible MHD in *Malara et al.*'s simulations. Also, the late time evolution of tearing instability studied by *Malara et al. [1992]* involved recurrent reconnection resulting from stretching of the X-point and generation of a new current sheet. We did not see any evidence of recurrent reconnection in the simulation run in Figure 2 nor was it seen in simulations of *Pritchett [1992]*. We have, however, seen it in our hybrid simulations, as we will demonstrate shortly.

[12] There are several mechanisms that can lead to the coalescence observed in Figure 2. One is the classical coalescence instability [e.g., *Finn and Kaw, 1977; Bhattacharjee et al., 1983*] based on the attraction of current pinches. The other is the stretching of the X-points [*Malara et al., 1992*]. *Malara et al.* argued that the chain of magnetic islands formed as the result of the tearing instability would be irregular. As a consequence, the weaker X-points are squeezed between pairs of magnetic islands and eventually disappear. A third possibility was raised by *Pritchett [1992]* where he found that the dominant effect is not the attraction of the current peaks but rather the development of current spikes on either side of the density depressions. In order to test these possibilities, we show in Figure 3 the evolution of the

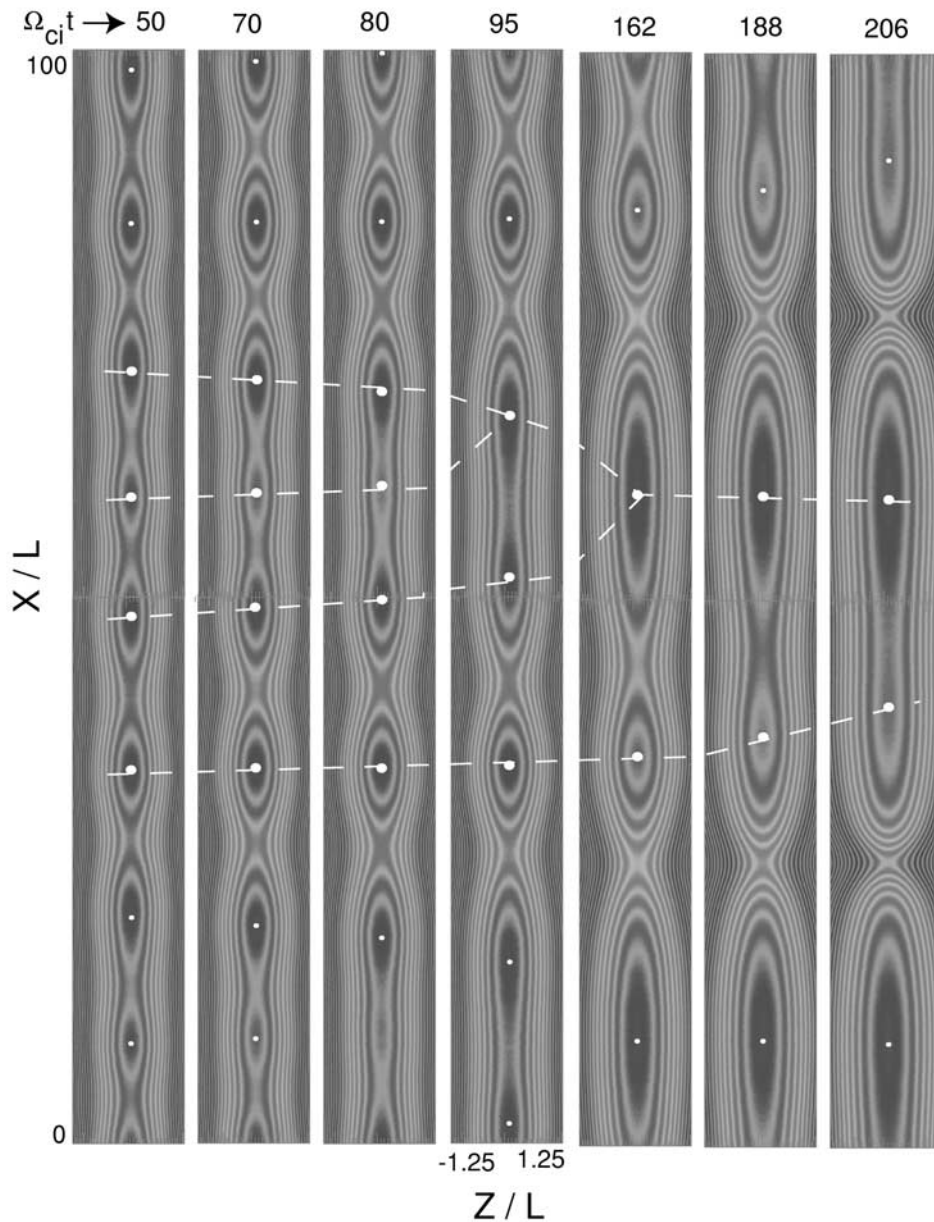


Figure 3. Harris run with seven unstable modes. Contour plot of A_y as a function of time. We have duplicated the contour plot at each time and overlaid it at the top of the original contour plot so that it would be easier to track the movement of the islands. See color version of this figure in the HTML.

magnetic islands in time, before the onset of the explosive phase. We have marked the center of each island with a white dot as a way to visualize the relative movement of the islands with respect to each other. In the first four time slices, the islands are all about the same size. As a result, they pair-wise coalesce due to attraction of their currents. In the last three panels, however, the islands sizes have become more irregular and the effect of flow from different X-points starts to play a more important role. However, none of the X-points stretch as suggested by Malara et al. to form unstable current sheets.

[13] The start of phase 4 signals the end of the coalescence stage as mode 1 has become dominant and shorter wavelength modes have started to grow. In Figure 4, we

have plotted the profiles of electron density and J_y at $z = 0$ at several times, starting with the time corresponding to start of phase 4 and ending with the time that is well into the explosive phase. At the first time slice, the density is seen to have a depression at the X-point whereas the current has its maximum. We also found the current to have its peak at the X-point at saturation for the one-mode and three-mode cases examined earlier. Use of small mass ratios as in the work of Pritchett [1992] can shift the peak current to the O-point [Paper II]. This again illustrates the need to use as large a mass ratio as possible. In contrast to the one-mode and three-mode cases above, in this case the density depression at the X-point continues to grow in size until finally a near vacuum is obtained. In the process the current

Table 2. Comparison Between Theoretical and Observed Linear Growth Rates for Three Harris Simulation Runs

Linear Properties	Single Mode Simulation		Three-Mode Simulation		Seven-Mode Simulation	
	Mode	γ/Ω_{ci}	Mode	γ/Ω_{ci}	Mode	γ/Ω_{ci}
Reverse Sheet Tearing						
$k_x L = 0.125$					1	0.057
$\gamma/\Omega_{ci} = 0.0525$						
$k_x L = 0.25$			1	0.0875	2	0.05
$\gamma/\Omega_{ci} = 0.0875$						
$k_x L = 0.375$					3	0.085
$\gamma/\Omega_{ci} = 0.107$						
$k_x L = 0.5$	1	0.113	2	0.089	4	0.11
$\gamma/\Omega_{ci} = 0.113$						
$k_x L = 0.625$			3	0.089	5	0
$\gamma/\Omega_{ci} = 0.106$						
$k_x L = 0.75$					6	0.11
$\gamma/\Omega_{ci} = 0.0834$						
$k_x L = 0.875$					7	0
$\gamma/\Omega_{ci} = 0.0494$						

develops a double peak structure along the $z = 0$ line and goes to zero in the vicinity of the X-point. At the edge of each spike in current, there exists a density pileup. Although there are similarities between the nonlinear evolution of tearing mode seen here and that reported by *Pritchett* [1992], there exist some differences. *Pritchett* [1992] found that mode 1 does not become dominant until well into the vacuum reconnection phase. Thus the dominant effect in his case was not the attraction of the current peaks but rather the

development of current spikes. In our simulation, however, there was a more clear separation between the coalescence phase and transition to the explosive phase. *Pritchett* [1992] used a simulation model where electrons simply provided a charge neutralizing background. That may be the cause of some of the differences observed here. The other factor may be that the detailed nonlinear evolution of tearing mode can change depending on the choice of parameters, number of active modes, etc.

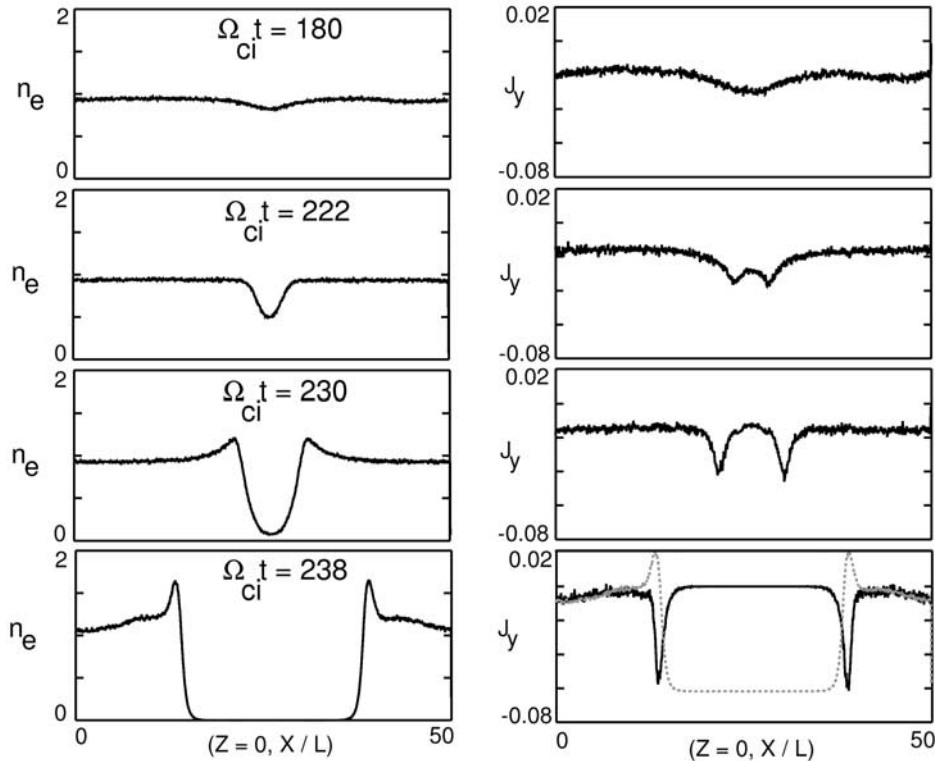


Figure 4. Harris run with seven unstable modes. Spatial profiles of the electron density and current density J_y at times beginning from the start of phase 4 and continuing into the explosive phase. In the last panel in J_y we have overlaid the profile of the electron density to illustrate the location of the density spikes relative to the spikes in the current.

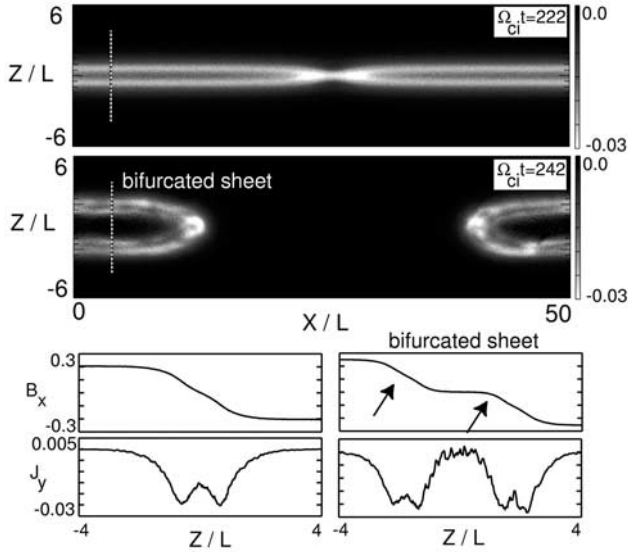


Figure 5. Harris run with seven unstable modes. (a)–(b) Intensity plot of J_y in phases 4 and 5 (Figure 2). (c)–(f) Profiles of B_x and J_y at the two slices marked in Figures 5a and 5b, respectively. The bifurcation becomes much more pronounced during the explosive phase of the tearing instability. See color version of this figure in the HTML.

[14] We saw in Figure 4 that J_y exhibits a bifurcated structure as one moves along the $z = 0$ from one side of the X point to the other side. A bifurcated structure is also seen in going across the current sheet. This is illustrated in Figure 5 which shows the snap shots of current J_y during phase 4 and phase 5 (see Figure 2). As reconnection proceeds to ion scales, the cone angle of reconnection opens up and the signatures of the bifurcated sheet become quite evident (Figures 5e–5f). This illustrates yet another mechanism, in addition to lower hybrid instability [Daughton *et al.*, 2004], ion/ion kink instability [Karimabadi *et al.*,

2003], and others, for generation of bifurcated current sheets and as such bifurcated structures may be more common than previously thought. The potential relevance of this finding to interpretation of bifurcated structures seen in the magnetotail [e.g., Runov *et al.*, 2003; Sergeev *et al.*, 2003] will be considered elsewhere.

4. Component Merging

[15] In this section, we limit our discussion to the strong guide field simulations. We have performed two simulations with the same parameters as in the antiparallel runs in section 3, except here we have introduced a guide field $B_{y0}/B_{x0} = 0.6$. In the three-mode case, modes 1 and 2 initially grow at close to their theoretical value (Table 3) but mode 3 does not grow much. As the islands coalesce, mode 1 becomes dominant but saturates at about 0.43 L, which is larger than the single mode case (Table 1) but is close to what we obtained for the three-mode Harris case.

[16] Next, we consider the case where there are seven linearly unstable modes in the system. Figure 6 shows the time evolution of the system in form of magnetic field lines. The islands are clearly seen to pair-wise coalesce until one large island is left. This evolution is somewhat different than that for the Harris case (Figure 3) where initially a small island was squeezed between two bigger islands and the two remaining islands were of much different size before they coalesced into one large island. Although details of the coalescence process depend on the properties of the linear modes that are initially excited, its main features remain intact: it mainly shuffles the power between the various modes and into the longest wavelength mode in the system and it is a rather slow process.

[17] The linear growth rate for the seven modes and their measured value from the simulation are listed in Table 2. Of the seven linearly unstable modes, only modes 2 and 4 initially grow as indicated by phase 1 in Figure 7. As islands coalesce, mode 4 saturates while mode 1 starts to grow at its theoretical (linear) rate (phase 2 in Figure 7). During this phase, the growth of mode 2 has slowed down by more than

Table 3. Comparison Between Theoretical and Observed Linear Growth Rates for Three Simulation Runs in the Strong Guide Field Limit^a

Linear Properties	Single-Mode Simulation		Three-Mode Simulation		Seven-Mode Simulation	
	Mode	γ/Ω_{ci}	Mode	γ/Ω_{ci}	Mode	γ/Ω_{ci}
Guide Field Tearing						
$k_x L = 0.125$					1	0
$\gamma/\Omega_{ci} = 0.0377$						
$k_x L = 0.25$			1	0.052	2	0.05
$\gamma/\Omega_{ci} = 0.0586$						
$k_x L = 0.375$					3	0
$\gamma/\Omega_{ci} = 0.0679$						
$k_x L = 0.5$	1	0.07	2	0.07	4	0.05
$\gamma/\Omega_{ci} = 0.0682$						
$k_x L = 0.625$			3	0	5	0
$\gamma/\Omega_{ci} = 0.0605$						
$k_x L = 0.75$					6	0
$\gamma/\Omega_{ci} = 0.0458$						
$k_x L = 0.875$					7	0
$\gamma/\Omega_{ci} = 0.0245$						

^aModes with zero growth rate are those that did not grow in the linear phase of the instability, although some growth in those modes appears in the nonlinear phase.

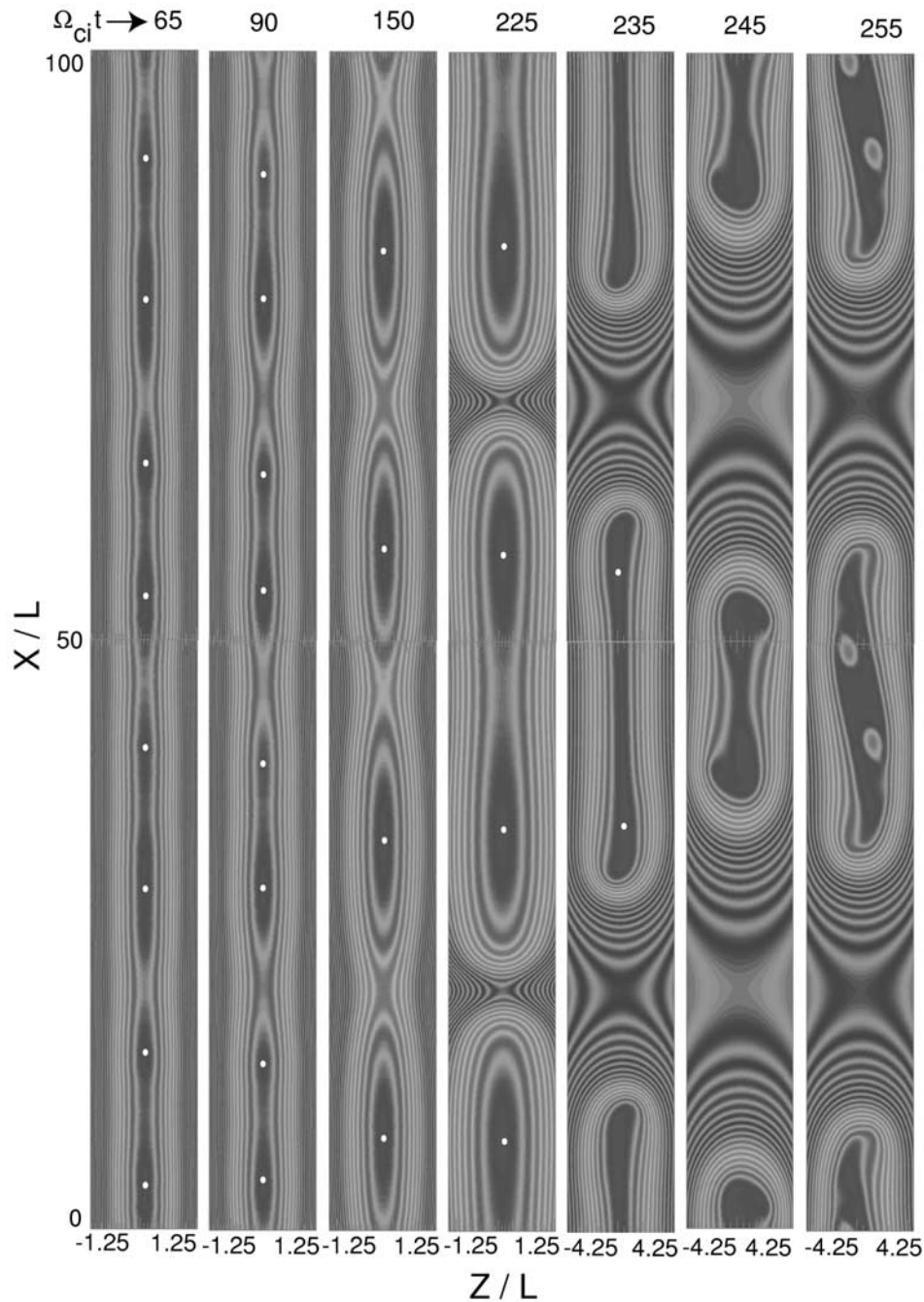


Figure 6. Guide field run with seven unstable modes. Contour plot of A_y as a function of time, showing pair-wise coalescence. We have duplicated the contour plot at each time and overlaid it at the top of the original contour plot so that it would be easier to track the movement of the islands. See color version of this figure in the HTML.

a factor of 2 from its linear rate. The next phase involves the continued growth of mode 1 and saturation of mode 2 until mode 1 finally becomes of the same amplitude as mode 2. At this time, the island has grown to about $0.7 L$ (Figure 7) and ion effects are starting to become important. In the next and final stage (phase 4 in Figure 7), the one remaining island grows at a rate larger than 3 times the linear phase and the system makes the transition to ion scales as we saw in Figure 2 for the Harris case. Thus the nonlinear evolution

of the tearing mode shows very similar behavior in the Harris and guide field regimes.

5. Effect of Electron Temperature Anisotropy

[18] There are reasons to expect finite electron temperature anisotropy within the current layer [e.g., *Daughton et al., 2004; Ricci et al., 2004; Karimabadi et al., 2004b*]. In this section we consider the effect of electron temperature

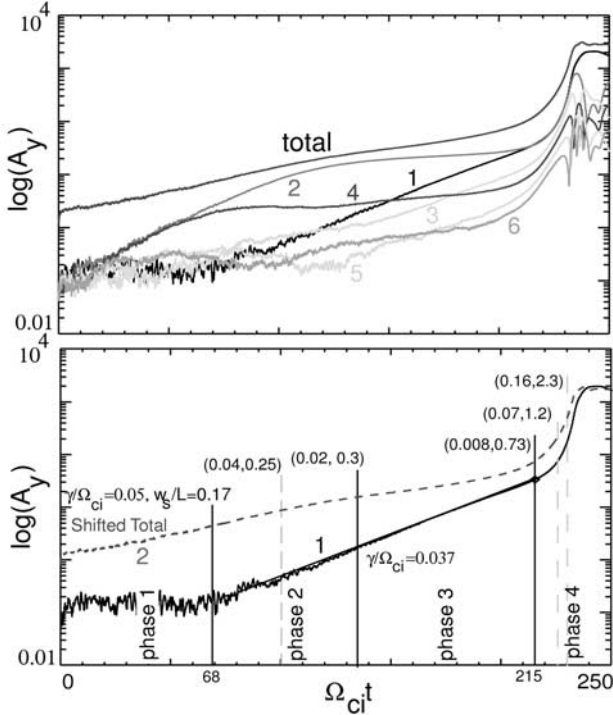


Figure 7. Guide field run with six unstable modes. (a) Time evolution of modes 1–6 as well as the sum of all the modes. (b) Fitting of the growth curve of mode 2 and 1 with exponential growth curves. Also shown is the island amplitude at each interval. The evolution of the system consists of four phases. (c) Time evolution of the electron temperature anisotropy. In the vacuum reconnection phase, temperature anisotropy is not defined and is not included in this figure. See color version of this figure in the HTML.

anisotropy on the tearing mode. Figure 8 shows the linear growth curve of the tearing mode for three different electron temperature anisotropies. The parameters in this figure are $m_i/m_e = 100$, $\omega_{pe}/\omega_{ce} = 5$, $T_i/T_{e\parallel} = 1$, and $\rho_i/L = 1.0$. This figure illustrates the sensitivity of the tearing mode to electron anisotropy. This dependence becomes even more exaggerated at realistic mass ratio [Paper II]. Note how a small $T_{\perp}/T_{\parallel} < 1$ greatly reduces the width of the spectrum of unstable modes and the growth rate, while a small $T_{\perp}/T_{\parallel} > 1$ increases the maximum growth by more than 15 times and shifts it to about 3 times shorter wavelength. For levels of $T_{\perp}/T_{\parallel} > 1$ expected to be generated by LHDI within the sheet ($\sim 10\%$), anisotropic tearing is the dominant instability in a neutral sheet [Karimabadi *et al.*, 2004b].

[19] The large linear growth rates caused by the presence of anisotropy enable us to perform a simulation that can simultaneously address a number of issues that would have been otherwise difficult in the isotropic limit. Specifically, we are interested in examining (1) the effect of anisotropy on the multimode tearing, (2) whether the picture of multimode evolution in Figures 2 and 7 remain intact or is modified when there are a large number of active modes in the system, (3) whether the presence of a background plasma can eliminate the vacuum reconnection phase, and

(4) whether the multimode case saturates. Accordingly, we performed a simulation with a 20% background density where both electron populations have $T_{\perp}/T_{\parallel} = 1.5$. The simulation box consists of 1280×1536 cells with 250 million particles per species, $\omega_{ce}\Delta t = 0.05$, and cell spacing of $0.13 c/\omega_{pe}$ in each direction. Other parameters are $\rho_i/L = 1.0$ and $T_i/T_{e\parallel} = 1.0$. The system size is large enough along the field direction to accommodate nine linearly unstable modes and wide enough across the sheet to allow study of the saturation.

[20] Figure 9a shows the time evolution of the first 10 modes, and the comparison of their initial growth rates with the linear theory are shown in Table 4. The initial evolution of the system is strongly determined by the level of noise in the simulation. Here, even during early phases the modes interact and there are strong deviations from the linear theory predictions. If we were to increase the number of particles per cell significantly so as to prolong the linear stage, we would expect to see closer match to linear theory. Given the large growth rates, however, the system would quickly get past the linear stage and mode-mode interactions would set in. Here modes 4–9 grow at substantially lower values than their linear growth rate. Modes 1–3 do not start a linear type of growth until after $\Omega_{ci}t \sim 2$, after which they grow much faster than their linear growth. This is due to the fact that the modes have started to coalesce to some extent already.

[21] Mode 1 becomes dominant early but the system does not go to one island until about $\Omega_{ci}t \sim 43$. Between $\Omega_{ci}t \sim 20$ and 38 , there is not much increase in saturation amplitude (coalescence) and mode 1 keeps growing while modes 2 and 3 saturate. However, by $\Omega_{ci}t \sim 38$, density at the x-point has been cut in half (Figure 9c) and the system starts a fast growth again. However, it never quite goes to a vacuum phase, as the density near the x line remains finite and the growth rate in late phases does not become as large as the linear phase. In fact by the time the density starts to decrease significantly near the x line (Figure 9c) at $\Omega_{ci}t \sim 49$, the

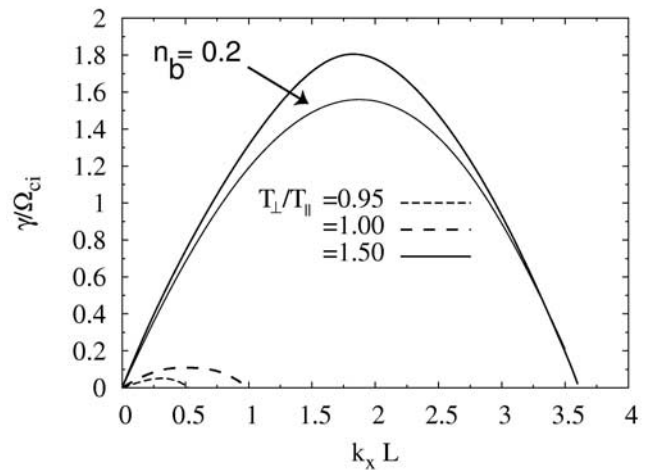


Figure 8. Linear growth curve of anisotropic tearing for three electron temperature anisotropies for $m_i/m_e = 100$, $\omega_{pe}/\beta_{ce} = 5$, $T_i/T_{e\parallel} = 1$, and $\rho_i/L = 1.0$. Also shown is the growth curve for $T_{\perp}/T_{\parallel} = 1.5$ in the presence of a uniform background with a density of 0.2.

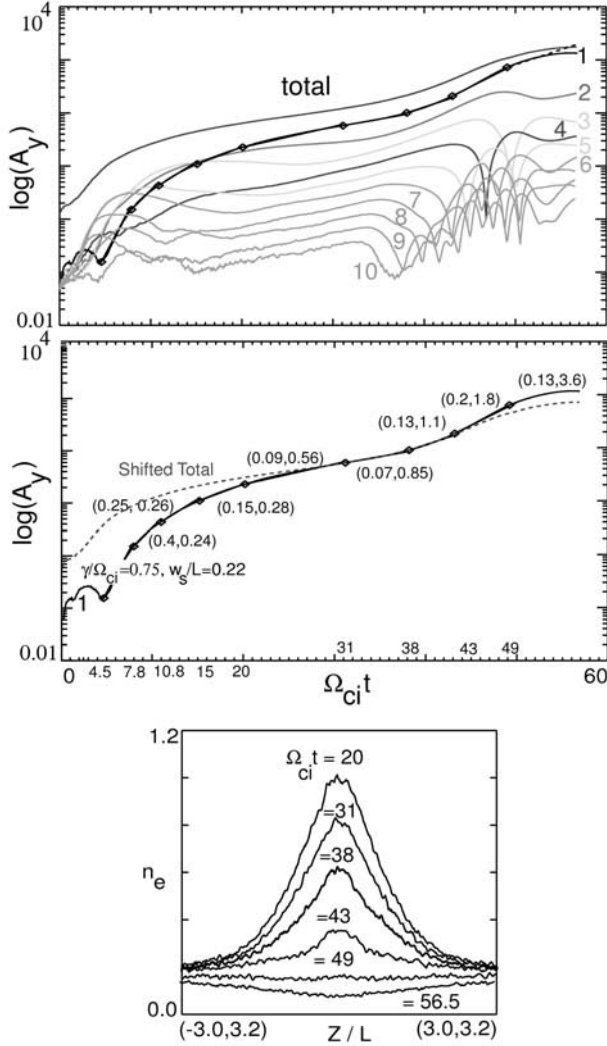


Figure 9. Anisotropic antiparallel simulation with nine unstable modes. (a) Time evolution of modes 1–10 as well as the sum of all the modes. (b) Fitting of the growth curve of mode 1 with exponential growth curves. Shown in parenthesis are the growth rate of mode 1 and island amplitude in each interval. (c) Time evolution of the electron density profile at $x/L = 3.2$. See color version of this figure in the HTML.

system is close to saturation and the growth rate is actually reduced. In the late phase of evolution in Figure 9, other modes are actually dropping in amplitude and bring down the total energy while mode 1 continues to grow. Had there been no background, the transition to the fast growth phase would have occurred sooner. We started with 20% background and it digs out to about 5%. So had we started with no background, the system would have dug out the region near the x-line to the vacuum limit.

[22] The apparent lack of a clear explosive phase is due to a number of factors. First, in the anisotropic case the growth rate is so large that even during the “slow” phase, mode 1 is growing at a rate (~ 0.1) not much slower than the explosive rate (~ 0.1 – 0.2) in the isotropic case. As a result, the system is already proceeding close to the vacuum limit. In fact, one may consider the period between $\Omega_{ci}t \sim 43$ and 49 where

mode 1 has a growth rate of 0.2 as the explosive phase. Second, the existence and duration of the explosive phase is tied to how close the system is to saturation by the time it starts to dig a “hole” near the X-point. In the present case, by the time the system starts to dig a hole in density, it is so close to saturation that the explosive phase is very short lived. The absence of a background population allows the system to reach the vacuum state sooner before the system nears saturation.

[23] The island half-width at saturation w_s is about $40 c/\omega_{pe}$, which corresponds to $k_x w_s \sim 1.25$, where k_x is the wave number for mode 1. This is in agreement with the observation of *Terasawa* [1981] that the saturation amplitude would satisfy the marginal stability condition $k_x w_s \sim 1$. *Pritchett* [1992] also found similar amplitude of $k_x w_s \sim 1.2$ in his simulation of coalescence instability. Our finding of similar saturation amplitude in the presence of an anisotropy indicates that this may be a general result. This finding is particularly relevant to a recent study by *Hau and Sonnerup* [1999] where they reconstructed the magnetic island structure at Earth’s magnetopause from the single-spacecraft data. *Hau and Chiou* [2001], by inspecting the field line map of this event, obtained the aspect ratio $k_x w_s/2\pi \sim 0.2$ for the magnetic island. Using resistive MHD, however, *Hau and Chiou* [2001] obtained an aspect ratio of 0.08 and speculated that inclusion of Hall term may lead to larger aspect ratio. Our finding of the saturation amplitude of $k_x w_s \sim 1.25$ ($k_x w_s/2\pi \sim 0.2$) is in very good agreement with the observed island aspect ratio at the magnetopause.

6. Fast Reconnection: Ion Scales

[24] It was recently shown [*Karimabadi et al.*, 2004a] that fast reconnection occurs even in the absence of the Hall term, purely due to ion kinetic effects. So the main role of electrons in the reconnection process is to allow the evolution to proceed to scales where the ions can take over. Thus the viability of any reconnection process at the magnetopause has to do with whether it can reach ion scales sufficiently fast. As an example, flux transfer events [*Russell and Elphic*, 1978] are of order of R_E in thickness normal to the magnetopause, or equivalently over 130 ion inertial lengths. Since full particle simulations can only be performed for relatively small systems, we have performed

Table 4. Comparison Between Theoretical and Observed Linear Growth Rates for the Run With an Initial Electron Temperature Anisotropy $T_{\perp}/T_{\parallel} = 1.5^a$

Wave Number	Mode	Linear Theory γ/Ω_{ci}	Simulation γ/Ω_{ci}	$\Omega_{ci}t$
$k_x L = 0.222$	1	0.329	0.79	4.8
$k_x L = 0.444$	2	0.65	1.1	4.3
$k_x L = 0.666$	3	0.911	0.99	3.1
$k_x L = 0.888$	4	1.154	0.7	1.9
$k_x L = 1.111$	5	1.354	0.85	1.0
$k_x L = 1.332$	6	1.51	1.15	1.8
$k_x L = 1.554$	7	1.611	0.47	1.4
$k_x L = 1.776$	8	1.658	1.1	1.7
$k_x L = 1.998$	9	1.649	0.85	1.1

^aThe last column shows the point in time at which linear growth changed slope.

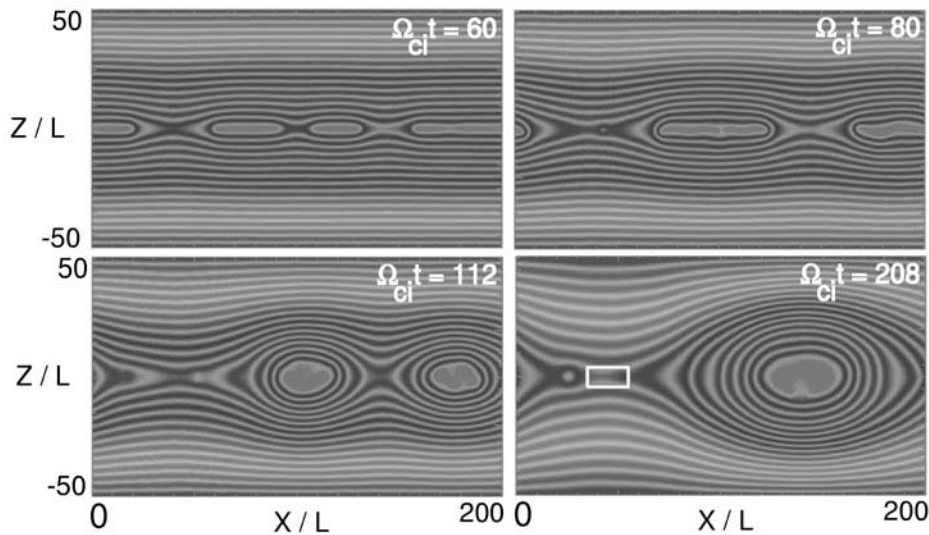


Figure 10. Contours of vector potential A_y for a hybrid simulation of multimode tearing at four different times. See color version of this figure in the HTML.

hybrid (fluid electrons, particle ions) simulations to investigate the behavior of coalescence process in larger systems. Our simulation box is $100 \times 200 c/\omega_{pi}$ with cell width of $0.1 c/\omega_{pi}$ in each direction. Figure 10 shows the snapshot of magnetic field lines at four different times. The result seems qualitatively similar to the full particle simulations in Figures 2, 7, and 9 as islands coalesce until only one island is left. The size of the island at saturation satisfies the marginal stability condition $k_x w_s \sim 1$ as we found for the anisotropic run in Figure 9.

[25] There is, however, one major difference between the hybrid result in Figure 10 and the full particle results shown so far: the current sheet immediately preceding the one remaining island has thinned out and a small island is seen to have formed. As it turns out, in addition to the coalescence process, there is another process related to stretching of the current sheet in certain regions of the current layer that leads to recurrent, time-dependent reconnection. This can be seen by zooming in around the region in the current sheet between X of 35 and 55, as shown in Figure 11. In the top left panel, the current sheet is seen to have stretched to become quite thin. By $\Omega_{ci}t = 80$, this thin current sheet has reconnected and a large plasmoid is formed and ejected to the right of the X -point. A much smaller plasmoid is also seen formed moving to the left. We have found that typically only one large island is formed through this process and a second plasmoid either never forms or has a very small amplitude. As the large plasmoid moves away, the current sheet goes back to its stretched state ($\Omega_{ci}t = 92$). The stretching and subsequent thinning of the current sheet continues ($\Omega_{ci}t = 104$) until the sheet becomes thin enough to reconnect again ($\Omega_{ci}t = 116$). This recurrent behavior has some similarities to that reported in incompressible MHD simulations of the tearing mode [e.g., Malara *et al.*, 1992]. As the system evolves, a large plasmoid is formed at $\Omega_{ci}t = 124$ but now it is ejected to the right of the X neutral point. As it moves away, the sheet once again goes back to its stretched state. The cycle repeats in time but the size of the

resulting island varies during each cycle. The recurrent formation of plasmoids/flux tubes due to the stretching of the X neutral points may provide a possible explanation of why reconnection is at times time-dependent at the magnetopause, giving rise to FTEs. We emphasize that the nature of recurrent reconnection here is different than the multiple x -point model of Lee and Fu [1985]. The presence of multiple x -points leads to time-dependent reconnection simply because several islands are formed and interact with each other. However, the time-dependent behavior shown in Figure 11 is due to stretching of the x -point and subsequent formation of a plasmoid when the current sheet becomes thin enough. It is also interesting that we found that only a single, rather than a pair of magnetic structures, formed after the thin current layer became unstable each time as shown in Figure 11. A recent global MHD simulation that showed formation of FTEs [Fedder *et al.*, 2002] also exhibited this behavior.

[26] We have performed several other hybrid simulations with differing densities of the background plasma. The basic results remain intact, although the growth of the instability is reduced as the density of the background plasma is increased.

7. Application to Magnetopause

[27] Since it is not yet possible to perform three-dimensional simulations of the tearing mode at the magnetopause using realistic parameters (Paper II), we have taken great care to establish the underlying physics of the tearing mode and associated physical scales using combination of linear theory and full particle simulations. In this section, we rely on this gained knowledge and use scaling arguments to draw conclusions for realistic parameter regime.

7.1. What is the Demarcation Line Between the Antiparallel and Guide Field Limits?

[28] The exact antiparallel case is a null point in parameter space. In general, there would be a finite B_{y0} . So the

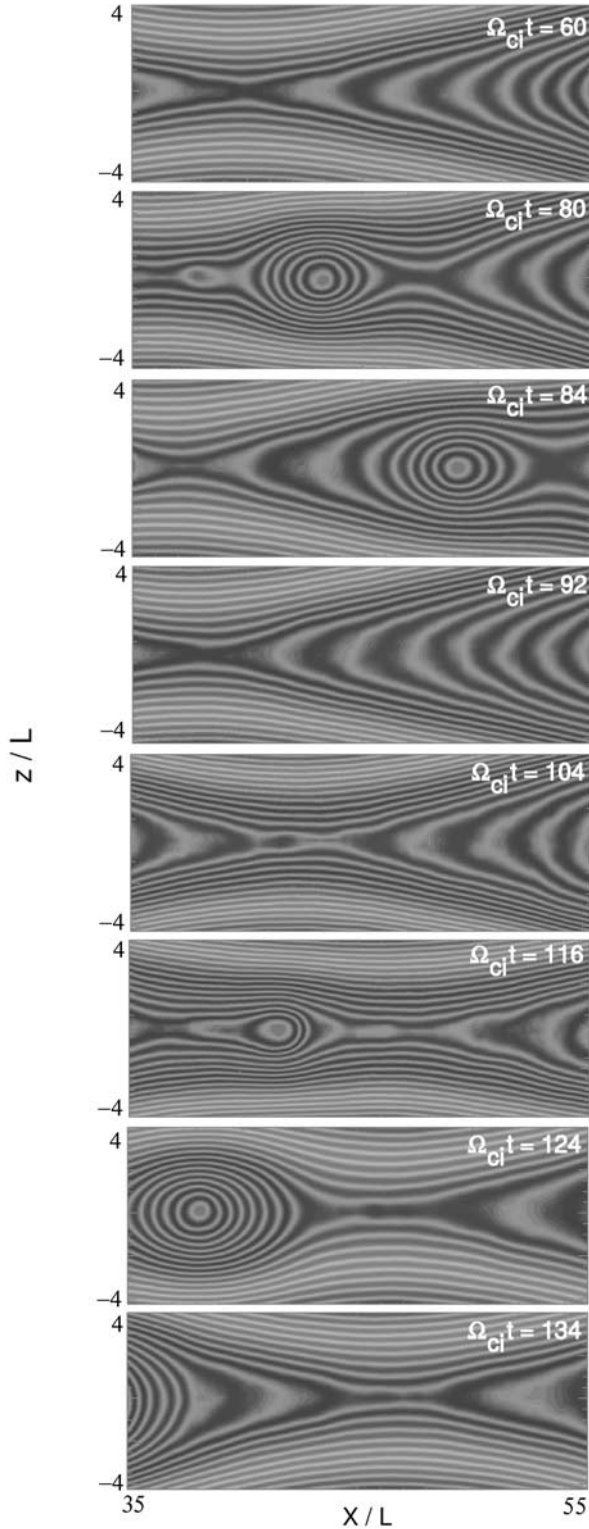


Figure 11. Intermittent reconnection. Time evolution of a zoomed-in region from Figure 10. See color version of this figure in the HTML.

relevant question is how large B_{y0} has to be in order to cause deviations in the linear properties of the tearing mode from the exactly antiparallel case. In Paper I, we found that the transition from antiparallel to guide field tearing occurs in

two stages, the intermediate regime and the strong guide field regime. The intermediate regime exists for a guide field in the range of $\sim 1-3 B_y^*$, where B_y^* is the value of guide field required to have a gyroradius comparable to the singular layer thickness in the antiparallel case. Figure 12 shows the contours of B_y^* as a function of T_i/T_e and ρ_i/L for $m_i/m_e = 1836$. For $T_i/T_e \sim 5$, which is the typical value at the magnetopause (dashed line in Figure 12), we see that B_y^*/B_{x0} ranges from ~ 0.025 to 0.07 for current sheet thickness ranging from 0.1 to 1 . Thus for typical magnetopause conditions it would take a small B_{y0} to transition into the guide field limit.

7.2. How Efficient is the Tearing Mode?

[29] One of the measures of the tearing efficiency is the comparison of its growth rate compared to the magnetosheath flow time from nose of the magnetopause to the equatorward edge of the polar cusp [e.g., *Quest and Coroniti*, 1981; *Gladd*, 1990]. *Quest and Coroniti* [1981] found sufficient growth time of tearing mode, whereas *Gladd* [1990] concluded that the growth rate was 1–2 orders of magnitude too small. Here we reconsider this problem using our linear code. Figure 13a shows the growth rate of the fastest mode (isotropic tearing) normalized to the convection time of 3 min as a function of the current sheet thickness for guide fields ($\alpha \equiv B_{y0}/B_0$) of 0, 0.05, 0.2, and 0.5 with $\omega_{pe}/\omega_{ce} = 100$. The three curves obtained from the linear code are very well fit by the following simple functions:

$$B_{y0}/B_{x0} = 0: \quad \gamma/\Omega_{ci} = 0.0351 * (\rho_i/L)^{2.3} \quad (1)$$

$$B_{y0}/B_{x0} = 0.2: \quad \gamma/\Omega_{ci} = 0.0171 * (\rho_i/L)^{2.6} \quad (2)$$

$$B_{y0}/B_{x0} = 0.5: \quad \gamma/\Omega_{ci} = 0.00991 * (\rho_i/L)^{2.9}. \quad (3)$$

Tearing mode growth rate is sensitive to the ratio of T_i/T_e and gets weaker for colder ions. Here we have taken $T_i =$

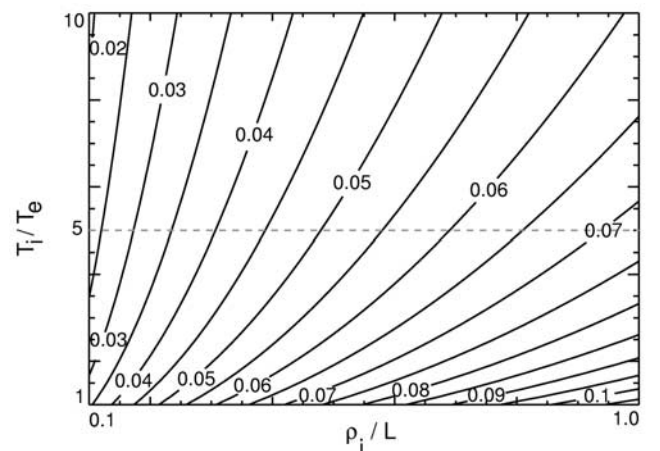


Figure 12. Contours of B_y^*/B_{x0} as a function of current sheet thickness and ion to electron temperature ratio for $m_i/m_e = 1836$.

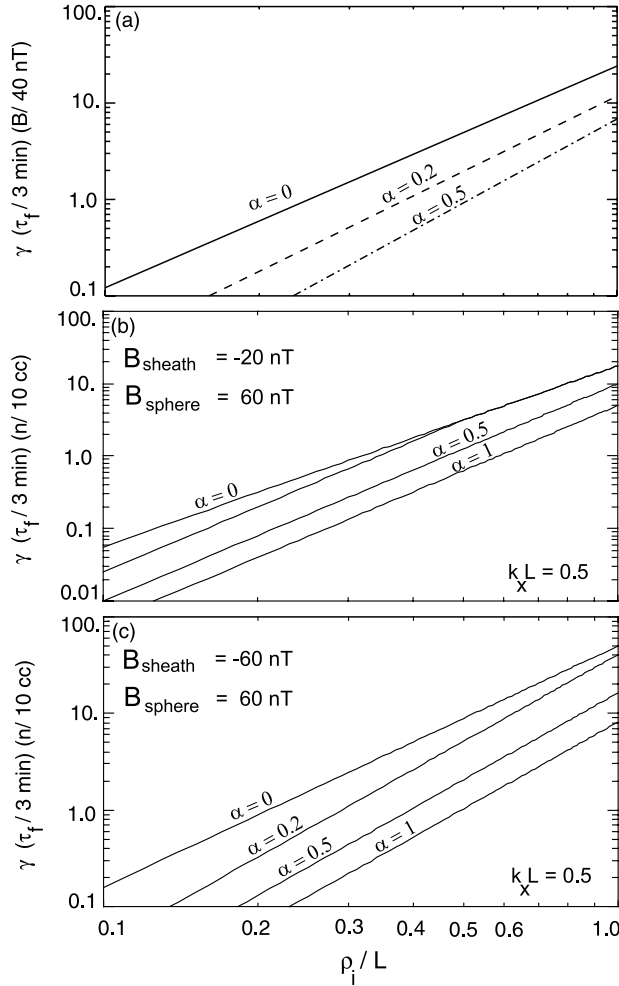


Figure 13. Graph of linear tearing growth rate normalized to the flow time from nose of the magnetopause to the equatorward edge of the polar cusp. Electrons and ions are assumed isotropic. (a) Harris equilibrium results using the linear Vlasov code. (b)–(c) Growth rates obtained from numerical solution to equations (4) and (5) for generalized equilibrium allowing for asymmetries. Other parameters are $m_i/m_e = 1836$, $\omega_{pe}/\omega_{ce} = 100$, and $T_i/T_e = 5$. Here α is defined as B_{y0}/B_{x0} .

$5T_e$ and used $B = 40$ nT which is the typical magnetosheath field. Appreciable growth requires $\gamma\tau_f \gg 1$. As Figure 13a indicates, only for thin current sheets isotropic tearing can grow sufficiently fast during the convection time. This calculation assumes that the mode would be able to e-fold several times at the linear pace and such is the best case scenario. However, even taking the nonlinear evolution of tearing into account, it appears that tearing has sufficient time to grow as long as the current sheet is thin. For example, we see from Figures 2 and 7 that it takes about $\Omega_{ci} t \sim 220$ for the system to evolve to an island width of $\sim L$, during which time the reconnected magnetic field $\delta B/B_0$ changes from its initial noise level of ~ 0.002 to ~ 0.1 . This time is about a factor of 2 smaller than the convection time, taking into account the fact that the growth rate of tearing decreases by $\sim 30\%$ when the mass ratio is increased from $m_i/m_e = 100$ – 1836 . In Figures 2 and 7, $T_i = T_e$ but for $T_i =$

$5T_e$ the tearing growth rate is reduced from $\gamma/\Omega_{ci} = 0.113$ to 0.035 . In that case, the nonlinear evolution of tearing may not be fast enough. However, in the anisotropic case (Figure 9), the evolution is accelerated to $\Omega_{ci} t \sim 40$ which is $\sim 1/12$ th of the convection time.

[30] The linear results here fall somewhere between those found by *Quest and Coroniti* [1981] and *Gladd* [1990]. *Quest and Coroniti* considered a generalized equilibrium which allowed for plasma and field asymmetries (see Appendix A). We have redone the calculations in their equilibrium, correcting several errors, and results are shown in Figures 13b and 13c. We fix the asymptotic magnetospheric field to be 60 nT, the ion and electron temperatures to be 500 eV and 100 eV, respectively, and the number density within the singular layer to be 10 cm^{-3} . In Figure 13b we assume that the southward component of the magnetosheath field is -20 nT, while in Figure 13c we assume it to be -60 nT. The parameter α is a measure of the magnetic shear and is defined to be the ratio of the guide field to the asymptotic magnetospheric field. Following *Quest and Coroniti* [1981], the analytic expression for the grow rate in the neutral sheet ($\alpha = 0$) limit is (see Appendix A):

$$\frac{\gamma_{NS}}{k_x v_{te}} \simeq \frac{1}{4} \frac{\Delta'}{d_e} \frac{c^2}{\omega_{pe}^2}, \quad (4)$$

while for the guide-field ($\alpha \neq 0$) we have

$$\frac{\gamma_{GF}}{k_x v_{te}} = \frac{1}{2\sqrt{\pi}} \frac{\Delta'}{l_s} \frac{c^2}{\omega_{pe}^2}. \quad (5)$$

The parameter Δ' is defined as the jump in the logarithmic derivative of the perturbed vector potential, and depends on the functional form of the shear field. In the work of *Quest and Coroniti* [1981] the form

$$C_1 + C_2 \tanh\left(\frac{x}{L}\right) \quad (6)$$

was chosen. If $C_1 = 0$, then

$$\Delta' = 2 \frac{1 - k^2 L^2}{k L^2}. \quad (7)$$

For the more general case of $C_1 \neq 0$ and moderate kL , Δ' is calculated numerically. In the results plotted (Figure 13), a few obvious features stand out. First, the neutral sheet limit yields the higher growth rate, and scales as $(\rho_i/L)^{5/2}$. The guide field limit scales as $(\rho_i/L)^3$ and thus falls off faster as the sheet thickens (as ρ_i/L decreases). The growth rate is linearly proportional to the electron number density, so rapid growth $\gamma\tau_f > 10$ can only be achieved by a combination of thin sheets and low densities. Finally, we note that the results plotted by *Quest and Coroniti* [1981] contain an error (a numerical factor of between 2 to 4). The correct results shown in Figures 13b–13c are in reasonable agreement with the Harris results in Figure 13a, indicating that asymmetries at the magnetopause are not expected to modify the results in a significant manner. Thus the two factors that have a major effect on $\gamma\tau_f$ in Figure 13 are the current sheet thickness and plasma density.

[31] The calculations in Figure 13 are based on isotropic conditions. Although antiparallel regime has faster growth, guide field tearing still provides sufficient growth for thin sheets. Ion anisotropy can increase the growth rate but only about a factor of ~ 2 for thin sheets. Electron anisotropy $T_{\perp}/T_{\parallel} > 1$, however, can significantly increase the growth rate of shorter wavelengths (e.g., Figure 8). Inclusion of electron anisotropy when there is a finite guide field is beyond the scope of this article and will be considered elsewhere. However, its effect is expected to be muted when there is a finite guide field. Thus the presence of any finite electron anisotropy with $T_{\perp}/T_{\parallel} > 1$ could favor antiparallel merging.

7.3. What Island Width is Required to Explain the Reconnected Rates at the Magnetopause?

[32] Aside from the linear growth, another measure of efficiency of the tearing mode is its nonlinear saturation. If the island saturation amplitude is small, then only a small fraction of magnetopause is open to reconnection and this leads to very small fraction of particles penetrating the magnetopause. In this section, we use simple arguments to derive an expression for the reconnected flux and its relation to the size of the island. The analysis here is valid for both the zero and finite guide field limits. For simplicity, let us assume a two-dimensional geometry in which the reconnection is restricted to the x - z plane. Further assume that the x-point is located at $x = z = 0$. Inflow is in the z direction, and outflow is in the x direction. Assume usual symmetries such that $U_z(x, 0, t) = U_x(0, z, t) = 0$, where \vec{U} is the electron velocity vector. For MHD, this quantity is also the ion velocity vector. We choose the electron velocity as it is more tightly bound to the magnetic field. For the time-dependent problem, a useful quantity is the total magnetic flux $\Phi(t)$ (per unit length in the y direction) that has been reconnected by time t , assuming a tangential discontinuity at time $t = 0$. We can define it as

$$\begin{aligned}\Phi(t) &= \int_0^{L_{\max}} B_z(x, 0, t) dx \\ &= \int_0^{L_{\max}} (\nabla \times \vec{A}) \cdot \hat{z} dx \\ &= \int_0^{L_{\max}} \frac{\partial}{\partial x} A_y(x, 0, t) \\ &= A_y(L_{\max}, 0, t) - A_y(0, 0, t)\end{aligned}\quad (8)$$

where L_{\max} is the maximum size of the system in the x -direction. If we define the reconnection rate as the total flux per unit time that has been reconnected, we get

$$\frac{d}{dt} \Phi(t) = \int_0^{L_{\max}} \frac{\partial}{\partial t} B_z(x, 0, t) dx \quad (9a)$$

$$= -c \int_0^{L_{\max}} (\nabla \times \vec{E}) \cdot \hat{z} dx \quad (9b)$$

$$= -c \int_0^{L_{\max}} \frac{\partial}{\partial x} E_y(x, 0, t) dx \quad (9c)$$

$$= -c E_y(L_{\max}, 0, t) + c E_y(0, 0, t). \quad (9d)$$

An alternate way to estimate the reconnection rate is

$$\frac{d}{dt} \Phi(t) \simeq \frac{\Phi(t + \Delta t) - \Phi(t)}{\Delta t} \quad (10a)$$

$$\Phi(t) = A_y(L_{\max}, 0, t) - A_y(0, 0, t). \quad (10b)$$

To make the example more concrete, define the magnetic field for the case of a magnetic island. Near the center of a one-dimensional sheared current layer, we can approximate the equilibrium magnetic field as linear in z (while pointing in x). We then obtain [Paper II] the following expressions for the total potential and the island half-width:

$$A_y(z) + \delta A_y(x) = -\frac{B_{x0}}{2L} z^2 - \frac{\delta B_n}{k_x} \cos(k_x x) \quad (11a)$$

$$\frac{w_s}{L} = 2\sqrt{\frac{\delta b}{k_x L}}, \quad (11b)$$

where we have defined $\delta b = \delta B_n/B_{x0}$. The x-points are located at $k_x x = 0$ (and $k_x x = 2\pi$), while the O-point is at $k_x x = \pi$. Thus the value of the vector potential at the x-point is ($x = z = 0$) is $\delta A_y(0) = -\frac{\delta B_n}{k_x}$. The reconnected flux (per unit length y) Φ can then be obtained as

$$\Phi(t) = \delta A_y(\pi/k_x) - A_y(0) = 2\frac{\delta B_n}{k_x} \propto (w_s/L)^2. \quad (12)$$

Thus the reconnected flux is proportional to the square of the half-width of the island. The reconnection rate is less straightforward to estimate analytically, since this now depends on the time history of the field. If, however, the island is exponentially growing with a growth rate γ , then we have

$$\frac{d\Phi(t)}{dt} = \gamma \Phi(t). \quad (13)$$

Note that there is an important distinction between the time-dependent reconnection rate as in (13) and the time-dependent reconnection rate. The latter is affected by both the linear and nonlinear evolution of the tearing mode whereas the steady state reconnection rate (see next section) is not. The time-dependent reconnection rate is generally lower in the presence of the guide field because both the linear growth and saturation amplitude are typically smaller.

[33] Reconnection rates are hard to measure at the magnetopause. There are several measures of reconnection rate. One is $M_{An} = V_n/V_A = \delta b$ [Paschmann, 1997] and another is the tangential electric field E_t measured in the frame moving with the magnetopause [Paschmann, 1997]. Lindqvist and Mozer [1990], using a statistical study of ISEE data, obtained an average value of E_t of 0.4 mV/m and an average convection speed of 20 km/s (Alfvén speed ~ 120 km/s). This translates to $\delta b \sim 0.07$ [Paschmann, 1997]. These are crude estimates but suffice for our purposes here. Using $\delta b \sim 0.07$ in (11b) and taking $k_x L = 0.5$, we obtain $w_s/L \sim$

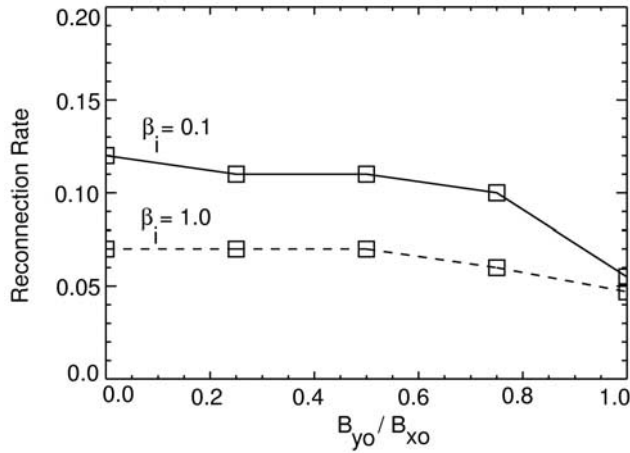


Figure 14. Steady state reconnection rate obtained from hybrid simulations of symmetric tangential discontinuities as a function of guide field for two different ion betas.

0.75. Thus in order to get sufficient reconnection, the magnetic island needs to grow to the scale length of the magnetopause L . In Paper II, we showed that single island tearing saturates at an amplitude at or below the singular layer thickness, which is much smaller than L . Thus multimode tearing is required to reconnect sufficient flux.

7.4. Effect of Guide Field on the Steady State Reconnection Rate

[34] Another way to gauge the viability of component merging at the magnetopause is to calculate the steady state reconnection rate (i.e., the rate calculated after the system has reached steady state) as a function of guide field strength. In a periodic simulation, the outflow jets that reach the boundary will start to come into the simulation on the opposite side. Thus, implementation of outflow boundary condition is required to allow the system to reach steady-state. We calculate the steady state reconnection rate using a procedure outlined by *Karimabadi et al.* [2004a]. We used two-dimensional (2-D) hybrid simulations of a symmetric tangential discontinuity [*Karimabadi et al.*, 1999] with a system size of 40×40 ion inertial length, and a single, localized resistivity of 10^{-4} (normalized to $4\pi/\omega_{pi}$) with a *cosh* profile extending two ion inertial lengths in each direction. For steady-state reconnection the definition $\Phi(t) = A_y(L_{\max}, 0, t) - A_y(0, 0, t)$ is still valid, but not useful. Here an assumption must be made regarding the relationship of the plasma motion and the magnetic field. We make the usual approximation that, away from the diffusion region, the magnetic flux is “frozen” into the electron fluid. It follows that

$$\frac{d}{dt}\Phi(t) = B_z(x, 0)U_x(x, 0) = -cE_y(x, 0). \quad (14)$$

Note that for a uniform reconnection rate to exist, we require that $E_y(x, z)$ be constant, independent of position. Finally, given the assumption that the flux and the electron velocity are tied to each other, an alternate way to define the reconnection rate is to define it as proportional to the asymptotic outflow velocity $U_x(x, 0)$.

[35] Figure 14 shows the steady-state reconnection rate normalized to upstream Alfvén velocity and magnetic fields $V_{Ao}B_o$, as a function of guide field for two initial conditions for the tangential discontinuity, one where ion beta is 0.1 and the other where ion beta is 1.0. Electron beta is 0.1 in both cases. In calculating the reconnection rate, we have verified that the magnitude of inflow U_zB_x and outflow U_xB_z match. At low beta, reconnection rate remains large and is only weakened somewhat when the guide field is equal to the background field. For a plasma beta of unity, the reconnection rate is reduced and demonstrates even a weaker dependence on the guide field for the range considered here. These results provide an independent verification that for modest values of guide field, component merging remains competitive with antiparallel merging. Note that in the presence of a uniform guide field, MHD would predict no change in the steady-state reconnection rate in 2-D. Both Hall effects and ion kinetics can in principle lead to dependence of reconnection rate on the guide field. We used our Hall-less hybrid code (Hall term is removed) [*Karimabadi et al.*, 2004a] to calculate the reconnection rate. We found no significant difference from the results shown in Figure 14. Thus we conclude that the dominant effect leading to the weak dependence of reconnection rate on the guide field in Figure 14 is ion kinetics.

7.5. What Size of Guide Field Does it Take to Have Equal Saturation Amplitude as the Harris?

[36] As we have argued and will show in the next section, in general there will be multiple linearly unstable modes at the magnetopause. However, the saturation amplitude of the single mode case provides another measure of efficiency of the tearing mode. It sets the base from which other effects (e.g., presence of multimodes) have to start. The lower the saturation amplitude of a single mode case, the harder it is for other processes to make the system reach ion scales. Accordingly, we now consider the parameter regime for which the single mode saturation amplitude of the antiparallel and guide field tearing are equal. We showed in Paper II that the single mode neutral sheet saturates at $\sim 2.9 \rho_e$ (much smaller than the singular layer thickness) unless there is a

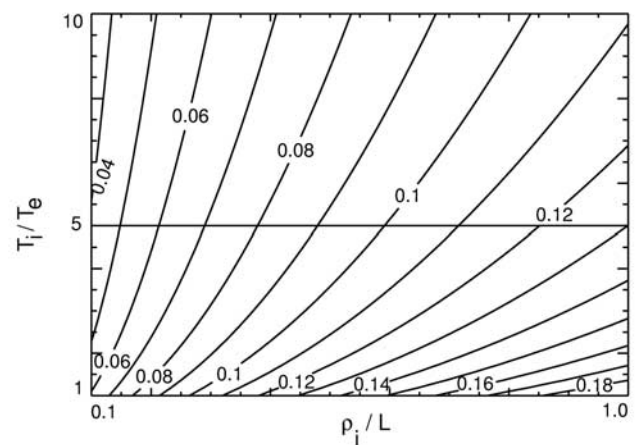


Figure 15. Parameter regimes where the singular layer thickness of antiparallel and guide field tearing become equal.

Tearing Mode at the Magnetopause

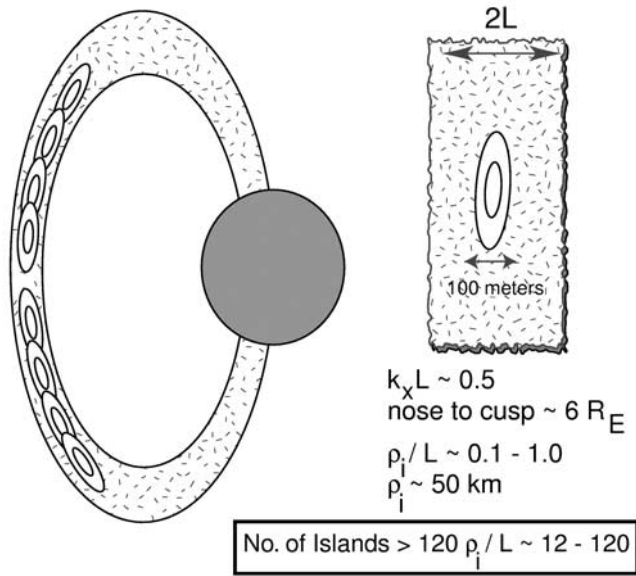


Figure 16. Schematic of multimode tearing instability at the magnetopause.

mechanism to pitch angle scatter the electrons at which point tearing would saturate at the singular layer thickness. In the guide field case, tearing saturates at the singular layer thickness, independent of the presence of scattering, and saturation amplitude is $\sim 1.8 \rho_{eG}$, where ρ_{eG} is the electron gyroradius in the guide field. Let us define the variable ζ to be the ratio of saturation amplitude of the antiparallel case to the singular layer thickness. Then, the guide field for which the saturation amplitude of the antiparallel and guide field cases become comparable is given by

$$B_{y_{\text{crit}}} = (1.8/\zeta)B_y^*, \quad (15)$$

where ζ is less than or equal to one. Figure 15 (for $m_i/m_e = 1836$) shows contours of $B_{y_{\text{crit}}}$ for $\zeta = 1$. Picking ζ for a particular case, this figure can then be used to easily estimate the guide field for which the two saturation amplitudes would be equal. For example, let us assume that it turns out that ζ is 0.5 rather than one for the parameters corresponding to the contour of 0.18 in Figure 15. That would mean that the guide field for which antiparallel and guide field tearing would have equal saturation amplitudes would be $0.18/\zeta = 0.36$. From Figure 15, it is clear that if there are no mechanisms to increase the saturation amplitude of the antiparallel case to the singular layer thickness so that $\zeta \ll 1$, then the guide field tearing can have larger saturation amplitude as long as the guide field is not too strong. Even for $\zeta \sim 1$, guide field tearing optimal region would remain competitive to antiparallel tearing for $\rho_i/L \sim 0.5-1$. In summary, antiparallel merging in 2-D would have $\zeta < 1$ and guide field tearing would be competitive unless the guide field is too strong.

7.6. How Many Modes Can Fit at the Magnetopause?

[37] We showed in Paper II that a single tearing mode saturates at too small of an amplitude. We demonstrated that the presence of many modes can overcome this stabilization. So here we examine how many modes can fit along the magnetopause. Figure 16 illustrates a simple calculation to determine the number of modes at the magnetopause. Taking the distance from nose to cusp to be about $6 R_E$ (Earth radii), current sheet thickness in the range of $\rho_i/L \sim 0.1-1.0$, with $\rho_i \sim 50 \text{ km}$, and using a typical wavelength for the tearing mode of $k_x L \sim 0.5$, we find that one can fit about $120 \rho_i/L$ islands along the magnetopause. This translates to about 12 modes when $\rho_i/L \sim 0.1$ and 120 modes when $\rho_i/L \sim 1$. Reconnection is clearly much more efficient for thin sheets since tearing has larger linear growth rates but also because there are more active modes in the system. The presence of any anisotropy in the electrons can shift the most unstable tearing modes to even shorter wavelengths, thus increasing the number of modes that can fit along the magnetopause. For example, for anisotropy of 1.1, the maximum growth shifts down to a wavelength that is more than a factor of 8 ($k_x * L = 0.4$ for realistic mass ratio) smaller than the isotropic case. This would dramatically increase the number of modes that can overlap. As we argue in the next section, the effect of anisotropy on tearing may be muted in the presence of a guide field. This statement, which needs to be verified by subsequent detailed calculations, if true, would heavily favor antiparallel merging in circumstances where LHDI can be operational. Note that ion anisotropy for thin sheets does not change the number of unstable modes significantly for thin sheets with $\rho_i \sim L$.

[38] In reality, reconnection is much more localized but the above simple calculation illustrates the point that under wide range of conditions at the magnetopause, more than one unstable tearing mode would be active. Electron physics controls how the frozen-in condition is broken and can limit the saturation limit. To obtain any reasonable reconnection rate at the magnetopause, however, reconnection has to get past the electron scales and into ion scales. Once ions dominate the reconnection process, fast reconnection is obtained [Karimabadi *et al.*, 2004a]. The transition to ion scales needs to happen on scales fast enough compared to convection time from the nose to equatorward of magnetopause. We found that a single tearing mode saturates at very small amplitudes (electron scales) regardless of whether there is a guide field or not. Thus unless there are other mechanisms that can significantly affect the growth rate and the resulting saturation of tearing (see below), single mode tearing is not likely to occur at the magnetopause. In the presence of several linearly unstable modes, which is expected to be the case at the magnetopause (Figure 16), the system goes through several phases (e.g., Figure 2) while transitioning to ion scales. Island amplitude at the end of Phase 1 (e.g., Figure 2) is a function of the number of linearly unstable modes in the system and can reach ion scales if there is sufficient number of modes. Details of the coalescence phase in Figure 2 (phases 2 and 3) are highly dependent on the island amplitudes at the end of phase 1. In Figure 2, the island amplitude has nearly doubled by the end of phase 3 but it took a very long time. So the maximum efficiency occurs for cases where the island width is

sufficiently close to ion scales so that the duration of phases 2 and 3 are minimized.

[39] There are several limitations to our study here that can affect the above results as we now consider.

7.6.1. Three-Dimensional (3-D) Effects

[40] Three-dimensional effects can alter the nonlinear evolution of tearing mode in two ways. First, there are current sheet instabilities in the plane outside of the tearing plane. Examples include ion/ion kink instability [e.g., *Karimabadi et al.*, 2003, and references therein] and lower-hybrid drift instability (LHDI) [e.g., *Buchner and Kuska*, 1999; *Lapenta et al.*, 2003; *Lapenta*, 2003; *Scholer et al.*, 2003; *Daughton et al.*, 2004; *Ricci et al.*, 2004]. Of the various current instabilities, LHDI is perhaps the most likely to affect the tearing mode [*Karimabadi et al.*, 2004b]. LHDI has been observed and it has been considered as a source of anomalous resistivity at the magnetopause (e.g., see review article by *Sibeck et al.* [1999]). *Daughton et al.* [2004] showed that LHDI generates electron temperature anisotropy with $T_{\perp}/T_{\parallel} \sim 1.1$ within the current sheet. *Karimabadi et al.* [2004b] showed that anisotropic tearing is the primary unstable mode operating within the current layer in the presence of $T_{\perp}/T_{\parallel} > 1$ and suggested a scenario where LHDI generates a finite electron anisotropy within the current layer [*Daughton et al.*, 2004], this in turn leads to anisotropic tearing with large growth rate at short wavelengths ($k_x L \gg 0.5$). The short wavelength modes coalesce, giving rise to fast reconnection (Figure 9) and overcoming the single mode stabilization.

[41] The extension of this work to finite guide field limit will be addressed elsewhere and requires construction of a new equilibrium. There are, however, reasons to expect effects of electron anisotropy on tearing to be muted in the presence of a guide field. In an unmagnetized plasma, there exists the Weibel instability [*Weibel*, 1959] which propagates in the direction of the lower temperature and has zero frequency. When $T_{\perp}/T_{\parallel} > 1$, the Weibel instability would grow in the parallel direction. In the absence of a guide field, the Weibel instability in the field free region would have the same (zero) frequency and propagation angle as the tearing mode and both would be driven by the Landau resonance. This allows the two modes to couple and merge [*Karimabadi et al.*, 2004b], resulting in the anisotropic tearing instability. In the presence of a finite guide field, however, electrons become magnetized within the current layer and Weibel instability ceases to exist. It is not clear whether the electron mirror mode can couple to tearing in such a case. Furthermore, the magnetization of electrons in the sheet allows the whistler anisotropy instability [e.g., *Gary*, 1993] to be operative (is a cyclotron resonance instability). This instability has a fast growth rate and may isotropize the electrons before tearing has a chance to grow significantly. Note also that the whistler anisotropic instability would have finite frequency and propagates in the direction of the local guide field. These properties are too different to allow merging of the mode with tearing. This apparent lack of coupling to other anisotropy driven modes would indicate that guide field tearing would remain weakly affected by the presence of anisotropy. Also since the presence of the guide field allows other fast growing anisotropy driven instabilities to exist within the current

layer, they would compete with the tearing mode and could isotropize the electrons too rapidly for reconnection.

[42] On the basis of the foregoing, we conclude that in the absence of electron temperature anisotropy, both antiparallel and component merging are equally favored as long as the guide field is not too large. However, if electrons are driven anisotropic with $T_{\perp}/T_{\parallel} > 1$ due to LHDI or some other mechanism, then antiparallel merging is expected to become heavily favored. This latter point needs to be verified by a careful study of anisotropy driven modes in the presence of a guide field and is a critical issue for future study of magnetic reconnection at the magnetopause.

[43] Another 3-D effect is the fact that the resonance surfaces for guide field tearing reside on different planes as determined by the condition $\mathbf{k} \cdot \mathbf{B} = 0$ [*Galeev and Zelenyi*, 1978]. This results in islands having different orientations that can then overlap, leading to magnetic percolation [e.g., *Galeev et al.*, 1986]. Although magnetic percolation has been thought to be too slow for magnetopause [e.g., *Wang and Ashour-Abdalla*, 1994], two factors may make it more viable. First, we identified regions in parameter space (Figure 14) where the saturation amplitude of single mode tearing is the same for both antiparallel and guide field tearing. In such regions, any overlap of islands, which can only occur in the presence of a guide field, can enhance the reconnection rate in the component merging regime over the antiparallel regime. So although percolation may not be the primary driver for obtaining reconnection on ion scales, it may play a role in expanding the parameter regime where component merging can operate. Second, we showed in Paper I that maximum growth rate can occur at oblique angles in the intermediate regime. This, together with the fact that the growth rate of such obliquely propagating modes can be comparable to the case without a guide field, can further expedite the overlap of islands.

[44] On the basis of the foregoing discussion, we conclude that 3-D effects are likely to enhance the rate of reconnection at the magnetopause in both antiparallel and component merging scenarios. As such, inclusion of 3-D effects will somewhat modify the parameter regime for the dominance of the two reconnection models but will not rule out either of them.

7.6.2. Local Conditions

[45] In our study we assumed the same conditions for both antiparallel and component merging scenarios, with the only difference being the strength of the guide field. However, the conditions for antiparallel and component merging are not identical. The most notable difference is the flow. For subsolar reconnection, there is very little flow shear. By contrast, antiparallel merging sites tend to have large flow shears because they are located at higher latitudes or more to the flanks. The presence of flow shear is known to affect the growth of the tearing mode. In resistive MHD, reconnection ceases when the flow velocity parallel to the magnetic field becomes super-Alfvénic [e.g., *Chen et al.*, 1997; *Knoll and Chacon*, 2002]. In Hall MHD, however, reconnection can persist for higher flow velocities extending to the super-Alfvénic regime [*Chacon et al.*, 2003]. Thus the presence of flow, by virtue of changing the reconnection rate, can put stringent conditions on the required efficiency of the tearing mode as we discussed above. The detailed effect of shear flow on reconnection in the kinetic regime is

beyond the scope of this paper and will be presented elsewhere.

7.7. Observational Signatures

[46] There are several features of reconnection that may be useful as diagnostics in observations.

7.7.1. Nongyrotropic Electron Distribution Function

[47] In the antiparallel case, we found that the electron distribution function is nongyrotropic. Guide field, on the other hand, magnetizes the electrons, rendering them gyro-tropic. Observationally it is very difficult to measure the guide field. *Scudder et al.* [2002], using the Polar data, have made detection of departure from electron gyro-tropy in an event which they cite as having no guide field. This is consistent with our expectation of nongyrotropic electron distribution in the antiparallel case.

7.7.2. Recurrent, Intermittent Reconnection

[48] We found evidence for sporadic reconnection when there was more than one mode present: reconnection generates a plasmoid that grows to finite size and is then ejected and after some time, the process is repeated as another plasmoid is generated and ejected. This may be of relevance to the formation of flux transfer events [e.g., *Russell and Elphic*, 1978]. The details of this process will be considered elsewhere.

7.7.3. Current Bifurcation

[49] Evidence for current bifurcation has been reported in the literature [e.g., *Runov et al.*, 2003; *Sergeev et al.*, 2003]. The exact cause of such bifurcations remains somewhat controversial. Here we showed that magnetic reconnection can lead to significant bifurcation of the current sheet (e.g., Figures 4 and 5). Previously, we had also found that the ion/ion kink instability can lead to bifurcated structure in the current [*Karimabadi et al.*, 2003]. Although some of the observed bifurcations may not be related to reconnection events, our finding here suggests that current bifurcation can be generated by many different processes and may be a common feature of current sheets.

8. Summary

[50] In this and the two accompanying papers (Paper I and II), we addressed the viability of antiparallel (zero guide field) and component merging (finite guide field) at the magnetopause by taking the approach that collisionless tearing mode is the onset mechanism and then compared the detailed linear and nonlinear properties of tearing as a function of guide field. Some of the key findings relevant to the magnetopause are as follows.

[51] 1. Isotropic tearing mode has sufficiently large linear growth compared to convection time only for thin sheets of $\rho_V/L \sim 1.0$.

[52] 2. The presence of even small levels of electron temperature anisotropy with $T_{\perp}/T_{\parallel} > 1$ can significantly increase the linear growth rate of the tearing mode in the antiparallel case.

[53] 3. Tearing mode saturates at minute amplitudes regardless of whether there is a guide field or not, unless there are several unstable modes present in the system. At the magnetopause, however, one would expect several linearly unstable modes. The resulting nonlinear interaction in this case allows the system to get past the single mode

stabilization and into ion scale regime. This process is significantly expedited in the presence of electron anisotropy with $T_{\perp}/T_{\parallel} > 1$.

[54] 4. The multimode evolution can lead to intermittent reconnection and strong bifurcation of the current sheet.

[55] 5. It takes a very small guide field to transition away from the antiparallel tearing.

[56] 6. Component merging is competitive with antiparallel merging unless the guide field is too large (≥ 0.4) and/or if LHDI is present. In the presence of LHDI, antiparallel is expected to be favored.

[57] Finally, we identified two main limitations to our study. One was the neglect of 3-D effects, and the other was the assumption of similar local conditions for both antiparallel and component merging. We argued that 3-D effects are most likely to impact the evolution of antiparallel case. This is because in 3-D the lower-hybrid drift instability would be operational which would drive electron anisotropy within the current layer [*Daughton et al.*, 2004]. This in turn leads to excitation of small scale tearing modes with very fast growth rates which then coalesce and drive longer wavelength tearing modes [*Karimabadi et al.*, 2004b]. Local conditions can also have a dramatic effect on reconnection. For instance, the presence of a flow shear can (1) affect the growth of tearing mode, (2) can have a bearing on whether reconnection is steady or unsteady, and (3) under extreme conditions can even shut off reconnection. Since antiparallel merging sites tend to have large flow shears because they are located at higher latitudes or more to the flanks, we expect antiparallel merging to be affected more due to flow shear than component merging. This may have bearings on whether reconnection is steady or time-dependent. The studies of flow shear and its effect on reconnection have been mostly based on resistive MHD. We are currently investigating the effect of flow shears on reconnection in a collisionless plasma and will report our results elsewhere. In summary, under electron isotropic conditions, we expect both antiparallel and component merging scenarios to be viable candidates for reconnection at the magnetopause. Two effects that are yet to be considered can modify this conclusion. First, we expect antiparallel merging would be strongly favored in the presence of electron anisotropies generated due to LHDI or other mechanisms but since no one has considered the tearing mode in anisotropic plasma with a guide field, this expectation needs further study. Second, local conditions where these two reconnection scenarios would originate are quite different and that may favor one model over the other and determine whether steady-state reconnection can be achieved.

Appendix A: Linear Tearing for Generalized Conditions

A1. Tearing Mode Growth Rates

[58] Assuming that the constant ψ approximation is valid, the expressions for tearing in the both the guide field (identified with subscript “GF”) and neutral sheet (identified with subscript “NS”) limits are

$$\frac{\gamma_{GF}}{k_x v_{te}} = \frac{1}{2\sqrt{\pi}} \frac{\Delta'}{l_s} \frac{c^2}{\omega_{pe}^2} \quad (A1)$$

$$\frac{\gamma_{NS}}{k_x v_{te}} \simeq \frac{1}{4} \frac{\Delta'}{d_e} \frac{c^2}{\omega_{pe}^2}, \quad (\text{A2})$$

$$d_e = [2\rho_e L]^{1/2} \quad (\text{A14})$$

where

$$\omega_{pe}^2 = \frac{4\pi n_e(z_0)e^2}{m_e} \quad (\text{A3})$$

$$\Delta_{GF} = \frac{\gamma l_s}{k_x v_{te}} = \frac{1}{\sqrt{\pi}} \frac{1 - (k_x L)^2 \varepsilon_e^2}{k_x \beta_e}, \quad (\text{A15})$$

where

$$l_s = B_y \left[\frac{d}{dz} B_x(z_0) \right]^{-1} \quad (\text{A4})$$

$$\rho_e = \frac{m_e c}{e B_{x0}} v_{te}. \quad (\text{A16})$$

We can also use the relations

$$d_e = \left[\frac{2v_{te} m_e c}{e} / \frac{d}{dz} B_x(z_0) \right]^{1/2} \quad (\text{A5})$$

$$\frac{\omega_{pe}^2}{c^2} \rho_e^2 = \beta_e = \frac{T_e}{T_e + T_i} \quad (\text{A17})$$

and

$$\Delta' = \frac{1}{A_{1y}(z_{0+})} \frac{d}{dz} A_{1y}(z_{0+}) - \frac{1}{A_{1y}(z_{0-})} \frac{d}{dz} A_{1y}(z_{0-}), \quad (\text{A6})$$

and

$$\Delta' = 2 \frac{[1 - (k_x L)^2]}{k_x L^2} \quad (\text{A18})$$

where z_0 satisfies $B_x(z_0) = 0$, and Δ' is the difference in the logarithmic derivative of A_{1y} determined from the external (adiabatic) solution

to yield

A2. Growth Rate for Harris Model

[59] Assume that the magnetic field takes the form

$$\vec{B} = \hat{x} B_{x0} \tanh\left(\frac{z}{L}\right) + \hat{y} B_{y0} \quad (\text{A7})$$

and

$$n = n_e \operatorname{sech}^2\left(\frac{z}{L}\right), \quad (\text{A8})$$

such that

$$n_e(T_e + T_i) = \frac{B_{x0}^2}{8\pi} \quad (\text{A9})$$

T_e and T_i are constant and

$$\frac{8\pi}{B_{x0}^2} n_e(T_e + T_i) = \beta_e + \beta_i = 1. \quad (\text{A10})$$

Thus

$$\beta_e = \left(1 + \frac{T_i}{T_e}\right)^{-1}. \quad (\text{A11})$$

For this antisymmetric model we have $z_0 = 0$ and

$$\omega_{pe}^2 = \frac{4\pi n_e e^2}{m_e} \quad (\text{A12})$$

$$l_s = \frac{B_{y0}}{B_{x0}} L \quad (\text{A13})$$

$$\begin{aligned} \frac{\gamma_{GF}}{\Omega_{ci}} &= \frac{m_i k_x \rho_e \Delta' c^2}{m_e 2\sqrt{\pi} l_s \omega_{pe}^2} = \frac{m_i}{m_e} \left(1 + \frac{T_i}{T_e}\right) \frac{k_x L \Delta'}{2\sqrt{\pi} l_s} \rho_e^3 \\ &= \frac{m_i}{m_e} \left(1 + \frac{T_i}{T_e}\right) \frac{1 - (k_x L)^2 \lambda}{\sqrt{\pi}} \frac{\lambda}{l_s} \left(\frac{\rho_e}{L}\right)^3 \\ &= \frac{m_i}{m_e} \left(1 + \frac{T_i}{T_e}\right) \frac{1 - (k_x L)^2 B_{x0}}{\sqrt{\pi}} \frac{B_{x0}}{B_{y0}} \left(\frac{\rho_e}{L}\right)^3 \end{aligned} \quad (\text{A19})$$

$$\begin{aligned} \frac{\gamma_{NS}}{\Omega_{ci}} &\simeq \frac{k_x \rho_e \Delta' c^2}{4 d_e \omega_{pe}^2} = \frac{m_i}{m_e} \left(1 + \frac{T_i}{T_e}\right) \frac{k_x L \Delta'}{4 d_e L} \rho_e^3 \\ &= \frac{m_i}{m_e} \left(1 + \frac{T_i}{T_e}\right) \frac{1 - (k_x L)^2}{\sqrt{8}} \left(\frac{\rho_e}{L}\right)^{5/2} \end{aligned} \quad (\text{A20})$$

Finally, since

$$\varepsilon_j \equiv \frac{\rho_j}{L}, \quad (\text{A21})$$

it follows that

$$\varepsilon_e \equiv \frac{\rho_e}{L} = \left(\frac{T_e m_e}{T_i m_i}\right)^{1/2} \varepsilon_i \quad (\text{A22})$$

and

$$\begin{aligned} \frac{\gamma_{GF}}{\Omega_{ci}} &= \frac{m_i}{m_e} \left(1 + \frac{T_i}{T_e}\right) \frac{1 - (k_x L)^2 L}{\sqrt{\pi}} \frac{L}{l_s} \left(\frac{T_e m_e}{T_i m_i}\right)^{3/2} \varepsilon_i^3 \\ &= \left(\frac{m_e}{m_i}\right)^{1/2} \left(\frac{T_e}{T_i}\right)^{3/2} \left(1 + \frac{T_i}{T_e}\right) \frac{1 - (k_x L)^2 L}{\sqrt{\pi}} \frac{L}{l_s} \varepsilon_i^3 \end{aligned} \quad (\text{A23})$$

$$\begin{aligned} \frac{\gamma_{NS}}{\Omega_{ci}} &= \frac{m_i}{m_e} \left(1 + \frac{T_i}{T_e}\right) \frac{(1 - k_x^2 L^2)}{\sqrt{8}} \left(\frac{T_e m_e}{T_i m_i}\right)^{5/4} \varepsilon_i^{5/2} \\ &= \left(\frac{m_e}{m_i}\right)^{1/4} \left(\frac{T_e}{T_i}\right)^{5/4} \left(1 + \frac{T_i}{T_e}\right) \frac{(1 - k_x^2 L^2)}{\sqrt{8}} \varepsilon_i^{5/2} \end{aligned} \quad (\text{A24})$$

Note that the two growth rates are equal when

$$l_s = \frac{2}{\sqrt{\pi}} d_e. \quad (\text{A25})$$

In the neutral sheet limit, a more accurate description [Laval *et al.*, 1966] using exact orbits leads to a similar result to equation (A24) but the factor of $1/\sqrt{8}$ is replaced by ~ 0.65 :

$$\begin{aligned} \frac{\gamma}{\Omega_{ci}} &= 0.65 \frac{m_i}{m_e} \frac{\varepsilon_e^{5/2}}{\beta_e} (1 - k_x^2 L^2) \\ &= 0.65 \left(\frac{m_e}{m_i}\right)^{1/4} \left(\frac{T_e}{T_i}\right)^{5/4} \frac{\varepsilon_i^{5/2}}{\beta_e} (1 - k_x^2 L^2) \end{aligned} \quad (\text{A26})$$

To obtain an estimate of the maximum growth, we modify the original expression to allow for deviations from the constant ψ approx. We obtain

$$\begin{aligned} \frac{\gamma}{\Omega_{ci}} &= 0.65 \frac{m_i}{m_e} \frac{\varepsilon_e^{5/2}}{\beta_e} (1 - k_x^2 L^2) \\ &= 0.65 \left(\frac{m_e}{m_i}\right)^{1/4} \left(\frac{T_e}{T_i}\right)^{5/4} \frac{\varepsilon_i^{5/2}}{\beta_e} (1 - k_x^2 L^2) \end{aligned} \quad (\text{A27})$$

For the choice of $T_i/T_e = 5$ and $m_i/m_e = 1836$, we obtain

$$\frac{\gamma}{\Omega_{ci}} = 7160 \varepsilon_e^{5/2} (1 - k_x^2 L^2) = 0.0797 \varepsilon_i^{5/2} (1 - k_x^2 L^2) \quad (\text{A28})$$

A numerical solution for the growth rate shows that for $0.0001 < \varepsilon_i < 0.001$, we obtain

$$\frac{\gamma}{\Omega_{ci}} = 0.07 \varepsilon_i^{2.49}. \quad (\text{A29})$$

For $0.001 < \varepsilon_i < 0.01$, we obtain

$$\frac{\gamma}{\Omega_{ci}} = 0.063 \varepsilon_i^{2.47}. \quad (\text{A30})$$

For $0.01 < \varepsilon_i < 0.1$, we obtain

$$\frac{\gamma}{\Omega_{ci}} = 0.055 \varepsilon_i^{2.45}, \quad (\text{A31})$$

while for $0.1 < \varepsilon_i < 1.0$, we obtain

$$\frac{\gamma}{\Omega_{ci}} = 0.049 \varepsilon_i^{2.39}. \quad (\text{A32})$$

Thus the power law dependence asymptotes to 2.5 for small ε_i but does decrease for increasing ε_i . The $k_x L$ at maximum growth for $\varepsilon_i = 1$ is 0.36.

A3. Quest and Coroniti [1981]

[60] Next, we calculate the growth rates for the asymmetric case which is more representative of conditions at the magnetopause. The following presentation corrects several mistakes in the original work of Quest and Coroniti. We begin again with the expressions (A1) and (A2) for the growth rates

$$\frac{\gamma_{GF}}{k v_{te}} = \frac{1}{2\sqrt{\pi}} \frac{\Delta' c^2}{l_s \omega_{pe}^2} \quad (\text{A33})$$

$$\frac{\gamma_{NS}}{k v_{te}} \simeq \frac{1}{4} \frac{\Delta' c^2}{d_e \omega_{pe}^2}. \quad (\text{A34})$$

The field model is

$$B_x(x) = C_1 + C_2 \tanh\left(\frac{z}{L}\right). \quad (\text{A35})$$

The null point $B_x(z_0) = 0$ satisfies

$$\frac{z_0}{L} = a \tanh\left(-\frac{C_1}{C_2}\right) = \frac{1}{2} \log\left(\frac{1-R}{1+R}\right) \quad (\text{A36})$$

where $R \equiv C_1/C_2$. Note that $|C_1/C_2| < 1$ is required for a null point to exist. The derivative for the B field is

$$\frac{d}{dz} B_x(x) = \frac{C_2}{L} \operatorname{sech}^2\left(\frac{z}{L}\right) \quad (\text{A37})$$

$$\frac{d}{dz} B_x(z_0) = \frac{C_2}{L} \operatorname{sech}^2\left(\operatorname{arc} \tanh\left(-\frac{C_1}{C_2}\right)\right) = \frac{C_2}{L} (1 - R^2) \quad (\text{A38})$$

Useful plasma parameters are $\omega_{ce} = \frac{e C_2}{m_e c}$, $\rho_e = \frac{v_{te}}{\omega_{ce}}$, $\varepsilon_e = \frac{\rho_e}{L}$, $\varepsilon_i = \frac{\rho_i}{L} = \sqrt{\frac{m_i T_i}{m_e T_e}} \varepsilon_e$, and $\beta_e = \rho_e \frac{2\omega_{pe}^2}{c^2} = \frac{8\pi n_e(z_0) T_e}{C_2^2}$. Other useful parameters are

$$d_e = \left[2\rho_e C_2 / \frac{d}{dz} B_x(z_0)\right]^{1/2} = \left[\frac{2\rho_e L}{(1-R^2)}\right]^{1/2} \quad (\text{A39})$$

$$\alpha \equiv \frac{B_y}{C_2 - C_1} = \frac{B_y}{C_2} \frac{1}{1-R} \quad (\text{A40})$$

$$\begin{aligned} l_s &= B_{y0} / \frac{d}{dz} B_x(z_0) = \frac{B_{y0}}{C_2} \frac{L}{(1-R^2)} = \frac{C_2 - C_1}{C_2 - C_1} \frac{B_{y0}}{C_2} \frac{L}{(1-R^2)} \\ &= \frac{\alpha L}{1+R} \end{aligned} \quad (\text{A41})$$

The constant α is the ratio of the guide field to the asymptotic sheath field ($-B_x(-\infty) = C_2 - C_1$). We calculate Δ' in the long wavelength limit ($k^2 L^2 \ll 1$, but still assuming constant ψ) to obtain [Furth *et al.*, 1963]

$$\Delta' \simeq \frac{1}{k} \left(\frac{1}{L_+^2} + \frac{1}{L_-^2}\right) \quad (\text{A42})$$

where

$$L_+ = B_x(\infty) / \frac{d}{dz} B_x(z_0) = L \frac{C_1 + C_2}{C_2(1 - R^2)} = \frac{L}{1 - R} \quad (\text{A43})$$

$$L_- = B_x(-\infty) / \frac{d}{dz} B_x(z_0) = L \frac{C_1 - C_2}{C_2(1 - R^2)} = \frac{-L}{1 + R} \quad (\text{A44})$$

and thus

$$\Delta' \simeq \frac{1}{k_x L^2} \left[(1 - R)^2 + (1 + R)^2 \right] = \frac{2}{k_x L^2} [1 + R^2] \quad (\text{A45})$$

Finally, we can express the guide field growth rate as

$$\begin{aligned} \frac{\gamma_{GF}}{k_x v_{te}} &= \frac{1}{2\sqrt{\pi}} \frac{\Delta' c^2}{l_s \omega_{pe}^2} = \frac{1}{2\sqrt{\pi}} \frac{\Delta' \rho_e^2}{l_s \beta_e} = \frac{1}{2\sqrt{\pi}} \frac{1 + R}{\alpha L} \frac{2}{k_x L^2} [1 + R^2] \frac{\rho_e^2}{\beta_e} \\ &= \frac{1}{2\sqrt{\pi}} \frac{C_2}{B_{y0}} \frac{1 - R^2}{L} \frac{2}{k_x L^2} [1 + R^2] \frac{\rho_e^2}{\beta_e} \end{aligned} \quad (\text{A46})$$

yielding

$$\begin{aligned} \frac{\gamma_{GF}}{\Omega_{ci}} &= \frac{m_i}{m_e} \frac{1}{\sqrt{\pi}} \frac{C_2}{B_{y0}} \left(\frac{T_e m_e}{T_i m_i} \right)^{3/2} \frac{\varepsilon_i^3}{\beta_e} [1 - R^4] \\ &= \frac{1}{\sqrt{\pi}} \left(\frac{m_e}{m_i} \right)^{1/2} \left(\frac{T_e}{T_i} \right)^{3/2} \frac{C_2}{B_{y0}} \frac{\varepsilon_i^3}{\beta_e} [1 - R^4] \end{aligned} \quad (\text{A47})$$

In a similar way, we have for the neutral sheet calculation

$$\frac{\gamma_{NS}}{k_x v_{te}} \simeq \frac{1}{4} \frac{\Delta' c^2}{d_e \omega_{pe}^2} = \frac{1}{4} \left(\frac{1 - R^2}{2\rho_e L} \right)^{1/2} \frac{2}{k_x L^2} [1 + R^2] \frac{\rho_e^2}{\beta_e} \quad (\text{A48})$$

yielding

$$\frac{\gamma_{NS}}{\Omega_{ci}} = \frac{1}{\sqrt{8}} \left(\frac{m_e}{m_i} \right)^{1/4} \left(\frac{T_e}{T_i} \right)^{5/4} \frac{\varepsilon_i^{5/2}}{\beta_e} [1 - R^2]^{1/2} [1 + R^2]. \quad (\text{A49})$$

[61] **Acknowledgments.** The research of H. Karimabadi and K. B. Quest was supported by NASA SEC Theory Program NAG5-11754, NSF grant ATM-9901665, and a joint UCSD-Los Alamos IGPP grant. The research of W. Daughton was supported by the Los Alamos National Laboratory Directed Research and Development program (LDRD), the NASA Geospace Science program, and an IGPP grant. Computations were partially performed on our local NASHI PC cluster and the San Diego Supercomputer Center, which is supported by the National Science Foundation. We thank R. Elphic, D. Krauss-Varban, and J. Huba for valuable discussions.

[62] Shadia Rifai Habbal thanks the referee for the assistance in evaluating this paper.

References

- Bhattacharjee, A., F. Brunel, and T. Tajima (1983), Magnetic reconnection driven by the coalescence instability, *Phys. Fluids*, *26*, 3332.
 Biskamp, D., R. Z. Sagdeev, and K. Schindler (1970), Nonlinear evolution of the tearing instability in the geomagnetic tail, *Cosmic Electrodynamic*, *1*, 297.
 Buchner, J., and J. P. Kuska (1999), Sausage mode instability of thin current sheets as a cause of magnetospheric substorms, *Ann. Geophys.*, *17*(5), 604–612.
 Chacon, L., D. A. Knoll, and J. M. Finn (2003), Hall MHD effects on the 2D Kelvin-Helmholtz tearing instability, *Phys. Lett. A*, *308*, 187.

- Chen, Q., A. Otto, and L. C. Lee (1997), Tearing instability, Kelvin-Helmholtz instability, and magnetic reconnection, *J. Geophys. Res.*, *102*, 151.
 Coroniti, F. V., and K. B. Quest (1984), Nonlinear evolution of magnetopause tearing modes, *J. Geophys. Res.*, *89*, 137.
 Crooker, N. U. (1979), Dayside merging and cusp geometry, *J. Geophys. Res.*, *84*, 951.
 Daughton, W., and H. Karimabadi (2005), Kinetic theory of collisionless tearing at the magnetopause, *J. Geophys. Res.*, *A03217*, doi:10.1029/2004JA010751.
 Daughton, W., G. Lapenta, and P. Ricci (2004), Nonlinear evolution of the lower-hybrid drift instability in a current sheet, *Phys. Rev. Lett.*, *93*, 105004.
 Drake, J. F., and Y. C. Lee (1977), Nonlinear evolution of collisionless and semicollisional tearing modes, *Phys. Rev. Lett.*, *39*, 453.
 Fedder, J. A., S. P. Slinker, J. G. Lyon, and C. T. Russell (2002), Flux transfer events in global numerical simulations of the magnetosphere, *J. Geophys. Res.*, *107*(A5), 1048, doi:10.1029/2001JA000025.
 Finn, J. M., and P. K. Kaw (1977), Coalescence instability of magnetic islands, *Phys. Fluids*, *20*, 72.
 Furth, H. P., J. Killeen, and M. N. Rosenbluth (1963), Finite resistivity instabilities of a sheet pinch, *Phys. Fluids*, *6*, 459.
 Galeev, A. A., and L. M. Zelenyi (1978), Magnetic reconnection in a space plasma, *Theoretical and Computational Plasma Physics*, p. 93, Int. Atom. Energy Agency, Vienna.
 Galeev, A. A., M. M. Kuznetsova, and L. M. Zelenyi (1986), Magnetopause stability threshold for patchy reconnection, *Space Sci. Rev.*, *44*(1-2), 1–41.
 Gary, S. P. (1993), *Theory of Space Plasma Microinstabilities*, Cambridge Univ. Press, New York.
 Gladd, N. T. (1990), Collisionless drift tearing modes in the magnetopause, *J. Geophys. Res.*, *95*, 20,889.
 Gonzalez, W. D., and F. S. Mozer (1974), A quantitative model for the potential resulting from reconnection with an arbitrary interplanetary magnetic field, *J. Geophys. Res.*, *79*, 4186.
 Harris, E. G. (1962), On a plasma sheath separating regions of one directional magnetic field, *Nuovo Cimento*, *23*, 115.
 Hau, L. N., and S.-W. Chiou (2001), On the linear and nonlinear resistive tearing-mode instabilities, *J. Geophys. Res.*, *106*, 8371.
 Hau, L. N., and B. U. O. Sonnerup (1999), Two-dimensional coherent structures in the magnetopause: recovery of static equilibria from single-spacecraft data, *J. Geophys. Res.*, *104*, 6899.
 Karimabadi, H., D. Krauss-Varban, N. Omidi, and H. X. Vu (1999), Magnetic structure of the reconnection layer and core field generation in plasmoids, *J. Geophys. Res.*, *104*, 12,313.
 Karimabadi, H., P. L. Pritchett, W. Daughton, and D. Krauss-Varban (2003), Ion-ion kink instability in the magnetotail: 2. Three-dimensional full particle and hybrid simulations and comparison with observations, *J. Geophys. Res.*, *108*(A11), 1401, doi:10.1029/2003JA010109.
 Karimabadi, H., D. Krauss-Varban, J. Huba, and H. X. Vu (2004a), On magnetic reconnection regimes and associated three-dimensional asymmetries: Hybrid, Hall-less Hybrid and Hall MHD Simulations, *J. Geophys. Res.*, *109*, A09205, doi:10.1029/2004JA010478.
 Karimabadi, H., W. Daughton, and K. B. Quest (2004b), Role of electron anisotropy in the onset of magnetic reconnection, *Geophys. Res. Lett.*, *31*, L18801, doi:10.1029/2004GL020791.
 Karimabadi, H., W. Daughton, and K. B. Quest (2005), Physics of saturation of collisionless tearing mode as a function of guide field, *J. Geophys. Res.*, *A03214*, doi:10.1029/2004JA010749.
 Knoll, D. A., and L. Chacon (2002), Magnetic reconnection in the two-dimensional Kelvin-Helmholtz instability, *Phys. Rev. Lett.*, *88*, 21.
 Lapenta, G. (2003), A new paradigm for 3D collisionless magnetic reconnection, *Space Sci. Rev.*, *107*(1-2), 167–174.
 Lapenta, G., J. U. Brackbill, and W. Daughton (2003), The unexpected role of the lower hybrid drift instability in magnetic reconnection in three dimensions, *Phys. Plasmas*, *10*(5), 1577–1587.
 Laval, G., R. Pellat, and M. Vuillemin (1966), Instabilités électromagnétiques des plasmas sans collisions, paper presented at Conference on Plasma Physics and Controlled Nuclear Fusion Research, Int. Atom. Energy Agency, Vienna.
 Leboeuf, J. N., T. Tajima, and J. M. Dawson (1982), Dynamic magnetic X points, *Phys. Fluids*, *25*(5), 784–799.
 Lee, L. C., and Z. F. Fu (1985), A Theory of magnetic flux transfer at the earth's magnetopause, *Geophys. Res. Lett.*, *12*(2), 105–108.
 Lindqvist, P.-A., and F. S. Mozer (1990), The average tangential electric field at the noon magnetopause, *J. Geophys. Res.*, *95*, 17,137.
 Luhmann, J. G., R. J. Walker, C. T. Russell, N. U. Crooker, J. R. Spreiter, and S. S. Stahara (1984), Patterns of potential magnetic field merging sites on the dayside magnetopause, *J. Geophys. Res.*, *89*, 1739–1742.
 Malara, F., P. Veltri, and V. Carbone (1992), Competition among nonlinear effects in tearing instability saturation, *Phys. Fluids, B*, *4*, 3070.

- Paschmann, G. (1997), Observational evidence for transfer of plasma across the magnetopause, *Space Sci. Rev.*, *80*, 217.
- Pritchett, P. L. (1992), The coalescence instability in collisionless plasmas, *Phys. Fluids, B*, *4*, 3371.
- Quest, K. B., and F. V. Coroniti (1981), Tearing at the dayside magnetopause, *J. Geophys. Res.*, *86*, 3289.
- Ricci, P., J. U. Brackbill, W. Daughton, and G. Lapenta (2004), Influence of the lower hybrid drift instability on the onset of magnetic reconnection, *Phys. Plasmas*, *11*, 4489.
- Runov, A., R. Nakamura, W. Baumjohann, T. L. Zhang, M. Volwerk, H. U. Eichelberger, and A. Balogh (2003), Cluster observation of a bifurcated current sheet, *Geophys. Res. Lett.*, *30*(2), 1036, doi:10.1029/2002GL016136.
- Russell, C. T., and R. C. Elphic (1978), Initial ISEE magnetometer results: Magnetopause observations, *Space Sci. Rev.*, *22*, 681.
- Scholer, M., I. Sidorenko, C. H. Jaroschek, R. A. Treumann, and A. Zeiler (2003), Onset of collisionless magnetic reconnection in thin current sheets: Three-dimensional particle simulations, *Phys. Plasmas*, *10*, 3521.
- Scudder, J. D., F. S. Mozer, N. C. Maynard, and C. T. Russell (2002), Fingerprints of collisionless reconnection at the separator: I. Ambipolar-Hall signatures, *J. Geophys. Res.*, *107*(A10), 1294, doi:10.1029/2001JA000126.
- Sergeev, V., et al. (2003), Current sheet flapping motion and structure observed by Cluster, *Geophys. Res. Lett.*, *30*(6), 1327, doi:10.1029/2002GL016500.
- Sibeck, D. G., et al. (1999), Plasma transfer processes at the magnetopause, *Space Sci. Rev.*, *88*, 207.
- Sonnerup, B. U. O. (1974), Magnetopause reconnection rate, *J. Geophys. Res.*, *79*, 1546.
- Terasawa, T. (1981), Numerical study of explosive tearing mode-instability in one-component plasmas, *J. Geophys. Res.*, *86*, 9007.
- Wang, Z., and M. Ashour-Abdalla (1994), Simulation of magnetic field line stochasticity at the magnetopause, *J. Geophys. Res.*, *99*, 2321–2334.
- Weibel, E. S. (1959), Spontaneously growing transverse waves in a plasma due to an anisotropic velocity distribution, *Phys. Rev. Lett.*, *2*, 83.

W. Daughton, Department of Physics and Astronomy, University of Iowa, Iowa City, IA, USA.

H. Karimabadi and K. B. Quest, Department of Electrical and Computer Engineering, University of California, San Diego, 9500 Gilman Drive, La Jolla, CA 92093-0407, USA. (homa@ece.ucsd.edu)